

## Understanding generalized inversions of nuclear magnetic resonance transverse relaxation time in porous media

J. Mitchell and T. C. Chandrasekera

Citation: [The Journal of Chemical Physics](#) **141**, 224201 (2014); doi: 10.1063/1.4903311

View online: <http://dx.doi.org/10.1063/1.4903311>

View Table of Contents: <http://scitation.aip.org/content/aip/journal/jcp/141/22?ver=pdfcov>

Published by the [AIP Publishing](#)

---

### Articles you may be interested in

[Measurement of the true transverse nuclear magnetic resonance relaxation in the presence of field gradients](#)  
J. Chem. Phys. **139**, 074205 (2013); 10.1063/1.4818806

[Spatio-temporal anomalous diffusion in heterogeneous media by nuclear magnetic resonance](#)  
J. Chem. Phys. **135**, 034504 (2011); 10.1063/1.3610367

[Obtaining true transverse relaxation time distributions in high-field NMR measurements of saturated porous media: Removing the influence of internal gradients](#)  
J. Chem. Phys. **132**, 244705 (2010); 10.1063/1.3446805

[Pore-size evaluation by single-sided nuclear magnetic resonance measurements: Compensation of water self-diffusion effect on transverse relaxation](#)  
J. Appl. Phys. **97**, 043901 (2005); 10.1063/1.1833572

[Internal surfaces of porous media studied by nuclear magnetic resonance cryoporometry](#)  
J. Chem. Phys. **108**, 8195 (1998); 10.1063/1.476175

---

A promotional banner for AIP Applied Physics Reviews. On the left is a thumbnail of a journal cover for 'AIP Applied Physics Reviews' featuring a diagram of a device. The main part of the banner has a blue background with a bright light source on the right. The text 'NEW Special Topic Sections' is prominently displayed in white. Below this, on an orange background, it says 'NOW ONLINE' in yellow, followed by 'Lithium Niobate Properties and Applications: Reviews of Emerging Trends' in white. The AIP Applied Physics Reviews logo is in the bottom right corner.

**NEW Special Topic Sections**

**NOW ONLINE**  
Lithium Niobate Properties and Applications:  
Reviews of Emerging Trends

**AIP** Applied Physics  
Reviews

# Understanding generalized inversions of nuclear magnetic resonance transverse relaxation time in porous media

J. Mitchell<sup>1,a)</sup> and T. C. Chandrasekera<sup>2</sup>

<sup>1</sup>*Schlumberger Gould Research, High Cross, Madingley Road, Cambridge CB3 0EL, United Kingdom*

<sup>2</sup>*Department of Chemical Engineering and Biotechnology, University of Cambridge, Pembroke Street, Cambridge CB2 3RA, United Kingdom*

(Received 30 September 2014; accepted 21 November 2014; published online 9 December 2014)

The nuclear magnetic resonance transverse relaxation time  $T_2$ , measured using the Carr-Purcell-Meiboom-Gill (CPMG) experiment, is a powerful method for obtaining unique information on liquids confined in porous media. Furthermore,  $T_2$  provides structural information on the porous material itself and has many applications in petrophysics, biophysics, and chemical engineering. Robust interpretation of  $T_2$  distributions demands appropriate processing of the measured data since  $T_2$  is influenced by diffusion through magnetic field inhomogeneities occurring at the pore scale, caused by the liquid/solid susceptibility contrast. Previously, we introduced a generic model for the diffusion exponent of the form  $-ant_e^k$  (where  $n$  is the number and  $t_e$  the temporal separation of spin echoes, and  $a$  is a composite diffusion parameter) in order to distinguish the influence of relaxation and diffusion in CPMG data. Here, we improve the analysis by introducing an automatic search for the optimum power  $k$  that best describes the diffusion behavior. This automated method is more efficient than the manual trial-and-error grid search adopted previously, and avoids variability through subjective judgments of experimentalists. Although our method does not avoid the inherent assumption that the diffusion exponent depends on a single  $k$  value, we show through simulation and experiment that it is robust in measurements of heterogeneous systems that violate this assumption. In this way, we obtain quantitative  $T_2$  distributions from complicated porous structures and demonstrate the analysis with examples of ceramics used for filtration and catalysis, and limestone of relevance to the construction and petroleum industries. © 2014 AIP Publishing LLC. [<http://dx.doi.org/10.1063/1.4903311>]

## I. INTRODUCTION

There is a need to understand structure-transport relationships in heterogeneous systems in order to optimize industrial processes such as oil recovery,<sup>1</sup> catalytic reactions,<sup>2</sup> and medicinal drug delivery.<sup>3</sup> Nuclear magnetic resonance (NMR) offers a powerful toolbox for determining the transport of fluids in porous media<sup>4,5</sup> and the geometry of the confining structure.<sup>6</sup> The magnetic susceptibility contrast  $\Delta\chi$  that is an inherent property of heterogeneous materials distorts the uniform static  $B_0$  magnetic field used in the NMR measurement. In porous media these field variations, occurring on the length-scale of the pores, are called “internal gradients.” Magnetic susceptibility contrast limits the application of several NMR techniques including spectroscopy,<sup>7</sup> diffusion,<sup>8</sup> and imaging<sup>9</sup> to fluids in porous materials. The effects of internal gradients are also significant in the measurement of the transverse spin relaxation time  $T_2$ , which is widely used for structural characterization; spin relaxation is used to probe surface-to-volume ratio of porous media,<sup>10,11</sup> granular suspensions,<sup>12</sup> and emulsion droplets.<sup>13</sup> The standard Carr-Purcell-Meiboom-Gill (CPMG) pulse sequence<sup>14</sup> provides a rapid measure of the decay of transverse magnetization. For liquids, this decay is approximately exponential with a time constant  $T_2$ . However, the motion of molecules through mag-

netic field gradients, as governed by the self-diffusion coefficient  $\mathcal{D}$ , results in an enhanced rate of signal decay.<sup>15</sup> In porous media, the diffusive attenuation can dominate over relaxation processes occurring at the pore surface, leading to the observation of an effective relaxation time  $T_{2,\text{eff}}$ , which is not sensitive to the geometry of the confining structure.<sup>16</sup>

It is important to note that although longitudinal  $T_1$  relaxation processes are sensitive to confining geometry through diffusive processes,<sup>10</sup> measured  $T_1$  relaxation times are not influenced by diffusion through internal gradients.<sup>16,17</sup> Rapid  $T_1$  measurements are available in the laboratory.<sup>18</sup> However, the faster and more versatile CPMG measurement remains preferable especially for low field instruments and mobile systems.<sup>19</sup> For example,  $T_2$  measurements are included readily in two-dimensional (2D) correlations of diffusion<sup>20</sup> or relaxation time.<sup>21</sup> In petrophysics,  $T_2$  is considered the archetypal NMR measurement<sup>22</sup> and is often acquired in well logging applications due to the difficulties of obtaining  $T_1$  data with a moving logging tool.<sup>23</sup> As the strength of internal gradients is determined by  $\Delta\chi B_0$ , a weak magnetic field will reduce the effect of internal gradients. By necessity, logging tools utilize low field magnets; there are significant technical challenges associated with generating a strong magnetic field under the harsh environmental conditions of a well bore. To provide consistent spin physics in laboratory log calibration measurements, low field magnets ( $B_0 = 0.05$  T,  $\nu_0 = 2$  MHz for  $^1\text{H}$ ) have become the industry standard in core analysis.<sup>1</sup> Even at these field strengths, it is possible to encounter rock

<sup>a)</sup> Author to whom correspondence should be addressed. Electronic mail: JMitchell16@slb.com

formations that exhibit large susceptibility contrast.<sup>24</sup> Beyond petrophysics, there is significant interest in applying high field NMR methods to liquids in porous media,<sup>25</sup> where even small susceptibility contrasts will induce large internal gradients.

The CPMG experiment generates a series of  $n$  spin echoes, each separated in time by  $t_e$  (echo time). Previously, we introduced an approximation to the diffusion exponent in CPMG data of the form  $-ant_e^k$ , where  $a$  is a composite diffusion parameter and  $k$  describes the echo time dependence of the diffusion exponent;<sup>26,27</sup> see Sec. II for further details. Analytic expressions for  $a$  are known only in the limiting cases of  $k = 3$  or  $k = 1$ ; between these extremes, no analytic form currently exists.<sup>16</sup> A 2D numeric inversion of the CPMG data allows the distributions in  $a$  and  $T_2$  to be separated for a given  $k$ ; see Sec. III. The determination of the appropriate value of  $k$  is not, however, straight-forward. The validity of a chosen  $k$  was established by testing for a data collapse in the diffusive contribution to the CPMG data, i.e., the diffusive contribution to the CPMG signal was plotted against  $nt_e^k$  where the results obtained at various  $t_e$  overlaid on a single curve when  $k$  was chosen appropriately. The optimum power was found by generating a data collapse plot for a range of  $k$ . Unfortunately this method, as implemented in our previous work,<sup>26,27</sup> has several limitations:

1. The observation of a successful data collapse is based on the subjective opinion of the experimentalist.
2. A manual search of  $k$  to find the optimum value is inefficient, potentially inaccurate, and again relies on the judgment of the experimentalist.
3. The data collapse will fail if  $k$  is required to be a function of echo time to fit the measurements.
4. The data collapse will fail if the diffusion exponent contains multiple different echo time dependencies.

To overcome the first two limitations we introduce an automatic selection of  $k$  based on the generalized cross validation (GCV) score generated when inverting the CPMG data, see Sec. III B. The third and fourth limitations relate to situations where the assumption that a single  $k$  value describes the diffusion exponent is violated. The third limitation is inherent to the experimental method: to determine  $a$ ,  $k$ , and ultimately  $T_2$ , it is necessary to acquire CPMG data with a range of echo times. However, under certain conditions  $k$  can vary with  $t_e$ . This limitation is a subtle but potentially important point that has not been considered in detail previously; we do so here in Sec. IV B. The fourth limitation is important in heterogeneous materials, such as reservoir rocks, where a hierarchy of pore sizes exist. The appropriate value of  $k$  can vary with pore size, and so a single  $k$ -value may not be a suitable representation of the entire sample. We consider this situation in Sec. IV C. We demonstrate the application of our generalized inversion method in Sec. V using a water-saturated glass bead pack, porous ceramics, and a Portland limestone rock as example porous media. These samples are representative of industrially significant materials that have been studied previously by NMR. For example, silicate glass bead packs are used in chromatography<sup>28</sup> and are studied as a proxy for heterogeneous catalyst supports.<sup>2,4,29</sup> Porous ceramics are used in pottery,<sup>30</sup> construction,<sup>31</sup> filtration,<sup>32</sup> and

monolith supports for chemical reactors.<sup>33</sup> Carbonate (e.g., limestone) reservoirs are an important source of oil, particularly in the Middle East.<sup>34</sup> Quarried limestone is used in construction where water transport dictates the in-service performance of the material.<sup>35</sup> In future work, we will consider the interpretation of  $a$ - $T_2$  distributions in specific systems of industrial relevance, including catalysts and oil reservoir rocks.

## II. THEORY

When measuring the transverse relaxation of liquids in porous media, the relaxation rate of molecules adsorbed on a pore surface  $T_{2,\text{surf}}^{-1}$  is determined by the surface-to-volume ratio  $S/V$  of the pore and a sample-dependent relaxivity parameter  $\rho_2$  such that<sup>11</sup>

$$\frac{1}{T_{2,\text{surf}}} = \rho_2 \frac{S}{V}. \quad (1)$$

The observed relaxation rate in a single pore will be equal to the surface relaxation rate under certain conditions. Specifically, when  $1/T_{2,\text{surf}}$  is large compared to the bulk liquid relaxation rate and when relaxation occurs within the fast diffusion limit of Brownstein and Tarr<sup>11</sup> such that  $\rho_2 \ell_s / D \ll 1$ , where  $\ell_s$  is a characteristic pore size. However, if an internal gradient exists across the pore, an effective relaxation rate is observed instead. In the general case considered in this study

$$\frac{1}{T_{2,\text{eff}}} = \rho_2 \frac{S}{V} + at_e^{(k-1)}. \quad (2)$$

The composite parameter  $a$  contains contributions from the dimensionless groups  $Dt_e/\ell^2$  and  $\gamma g_{\text{eff}} \ell^3/D$ ,<sup>26</sup> where  $\ell$  is a diffusion length,  $g_{\text{eff}}$  is the effective gradient experienced by the spins, and  $\gamma$  is the gyromagnetic ratio. In general, the analytic form of  $a$  is unknown except that  $\sqrt[k]{a}$  has dimensions of inverse time. The echo time dependence is assumed to be constrained by  $1 \leq k \leq 3$  based on theoretical models of diffusion in restricted geometries.<sup>36</sup> The upper limit, where the diffusive exponent exhibits a cubic dependence on  $t_e$ , corresponds to free diffusion in a uniform magnetic field gradient. Any restriction of the diffusive motion of the nuclear spins is expected to cause motional narrowing. At the extreme limit of motional narrowing, the diffusive exponent becomes inversely proportional to diffusion coefficient and linear in echo time.

If a distribution of pore sizes exists within a sample, then a distribution of relaxation times  $g(T_2)$  will be present. In the pure relaxation case, the normalized signal (magnetization) associated with the  $n$ th echo is

$$\frac{S(nt_e)}{S(0)} = \int_{-\infty}^{\infty} \exp\left\{-\frac{nt_e}{T_2}\right\} g(T_2) d(\log_{10} T_2). \quad (3)$$

When generating a relaxation time distribution, it is usual to solve for  $g(T_2)$  on the  $\log_{10}$  scale, as indicated in the differential term. Diffusion through internal gradients on the time scale of the measurement will introduce an additional exponential term into Eq. (3). In most transverse relaxation time measurements of liquids in porous media, the surface relaxation and diffusion terms are encapsulated within a single

effective relaxation time, as modeled by Eq. (2), and so the data are fitted using the form

$$\frac{S(nt_e)}{S(0)} = \int_{-\infty}^{\infty} \exp\left\{-\frac{nt_e}{T_{2,\text{eff}}}\right\} g(T_{2,\text{eff}}) d(\log_{10} T_{2,\text{eff}}). \quad (4)$$

Here, we wish to separate the contributions to the observed relaxation time distribution. It is reasonable to assume that surface relaxation processes and diffusion through non-uniform magnetic fields are independent<sup>20</sup> such that

$$\frac{S(nt_e, t_e)}{S(0, 0)} = \int_{-\infty}^{\infty} \int_{-\infty}^{\infty} \exp\left\{-\frac{nt_e}{T_2}\right\} g(T_2) \exp\{-ant_e^k\} \times h(a) d(\log_{10} T_2) d(\log_{10} a), \quad (5)$$

where  $h(a)$  is a distribution of the composite diffusion parameter.

The diffusion behavior is governed by the relative magnitude of three length scales:

1. The diffusion path length  $\ell_e \approx (\mathcal{D}t_e/2)^{1/2}$  determined by the experimental echo time.
2. A characteristic pore size  $\ell_s$ .
3. A dephasing path length  $\ell_g \approx (\mathcal{D}/\gamma g_{\text{eff}})^{1/3}$  over which the Gaussian phase approximation for the spin ensemble breaks down.

If any of these length scales is less than the other two by at least an order of magnitude, diffusion will occur within a defined asymptotic regime, see Fig. 1. When  $\ell_e \ll \ell_s$  and  $\ell_g$  the short time (ST) regime is observed.<sup>37</sup> This regime typically corresponds to samples with large pores and a low magnetic susceptibility contrast (weak internal gradient), and is empirically similar to free diffusion in a constant gradient. In the ST regime,  $k = 3$  and  $a = \mathcal{D}\gamma^2 g_{\text{eff}}^2/12$ . This is the ideal regime for NMR measurements as the exponents in  $g_{\text{eff}}$  and  $T_2$  are separable<sup>38</sup> and an effective internal gradient distribution is calculable.<sup>39</sup>

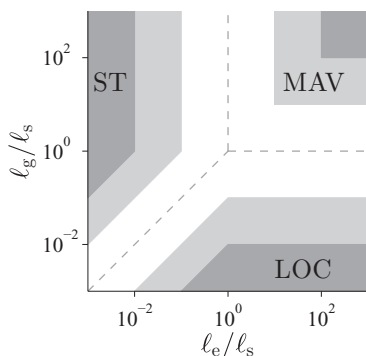


FIG. 1. Schematic illustrating the diffusion regimes ST, MAV, and LOC as defined by the length scales  $\ell_e$ ,  $\ell_s$ , and  $\ell_g$ . The dashed lines indicate equivalence of the length scales. The dark shaded areas indicate the regions where the asymptotic behavior is expected to apply, corresponding to one length scale being shorter than the others by at least two orders of magnitude. However, the exact limits of these asymptotes are not clearly defined. The maximum extent to which asymptotic behavior might be expected is shown by the light shaded areas, corresponding to one length scale being short than the others by at least an order of magnitude. Pre-asymptotic diffusion regimes apply outside of the shaded regions.

If  $\ell_s \ll \ell_e$  and  $\ell_g$  then the motional averaging (MAV) regime is relevant.<sup>40</sup> This regime is encountered in samples with very small pores where each spin explores the pore multiple times during  $t_e$  and hence becomes insensitive to the details of a non-uniform magnetic field across a pore. In the MAV asymptote,  $k = 1$  and  $a \approx \gamma^2 \bar{g}^2 \ell_s^4/120\mathcal{D}$ ,<sup>41</sup> where  $\bar{g}$  is the average gradient across a pore.

The localization (LOC) regime is applicable when  $\ell_g \ll \ell_e$  and  $\ell_s$ .<sup>36,42</sup> This regime is encountered in the presence of strong internal gradients. Spin dephasing occurs rapidly in localized regions, leading to a non-uniform magnetization profile across individual pores. The fraction of pore volume containing coherent spins is approximately  $\ell_g/\ell_s$ , which defines the maximum detectable signal. Hence, in this regime, the observed signal amplitude is determined by details of the magnetization profile and not the total liquid volume.<sup>16</sup> As with the MAV regime,  $k = 1$  in the LOC asymptote while  $a \approx (\gamma \Delta \chi B_0 \mathcal{D})^{1/2}/\ell_s$ .

In the limit that  $k = 1$  (corresponding to either the MAV or LOC regimes), the contributions to the signal decay in a CPMG experiment from relaxation and diffusion become indistinguishable. Outside the MAV or LOC asymptotes,  $1 < k \leq 3$  and a distribution  $h(a)$  can be determined with an appropriate choice of  $k$ . This distribution in  $a$  is used to reconstruct the diffusive contribution to the signal decay given by

$$\frac{S(nt_e, t_e)}{S(0, 0)} = \int_{-\infty}^{\infty} \exp\{-ant_e^k\} h(a) d(\log_{10} a). \quad (6)$$

The CPMG data may be divided by this empirical diffusive contribution to leave the pure relaxation decay, Eq. (3), which is inverted to obtain  $g(T_2)$ . However, such a division is prone to distorting the data through amplification of noise at long times. A better approach is the generation of the 2D distribution  $f(a, T_2)$  by inverting the CPMG data described in Eq. (5). Assuming  $a$  and  $T_2$  are independent,  $h(a)$  and  $g(T_2)$  are given directly by the marginal distributions

$$g(T_2) = \int_{-\infty}^{\infty} f(T_2, a) d(\log_{10} a), \quad (7a)$$

$$h(a) = \int_{-\infty}^{\infty} f(T_2, a) d(\log_{10} T_2). \quad (7b)$$

We adopt this approach in the current work. An appropriate 2D inversion process is reviewed next; a full review of 2D inversion methods has been presented in Ref. 43.

### III. INVERSION METHOD

It is usual to generate distributions of NMR relaxation or diffusion data on a  $\log_{10}$  scale and this processing is non-trivial. The first-kind Fredholm integral equations given in Sec. II have been expressed in this form already; note that the distribution  $f(a, T_2)$  obtained by inverting Eq. (5) is not the true density distribution due to the  $\log_{10}$  scaling.<sup>43</sup> The



acquired CPMG data are a sum of signal (magnetization) and noise (error), such that  $b(nt_e, t_e) = S(nt_e, t_e) + e(nt_e)$ . The data are acquired as a function of  $nt_e$  and  $t_e$  and stored in matrix  $\mathbf{B}$ . In order to generate a stable solution to this ill-posed problem in the presence of noise, the solution  $\hat{f}$  is constrained to be smooth, always positive, and bounded by finite values of  $a$  and  $T_2$ .

The measured data and estimated solution will contain a discrete number of values, so we can express the inverse problem in vector-matrix notation as

$$\mathbf{b} = \mathbf{K}\mathbf{f} + \mathbf{e}, \quad (8)$$

where  $\mathbf{b}$  is the data matrix  $\mathbf{B}$  stacked column-upon-column as a vector,  $\mathbf{K}$  is a kernel matrix which represents the expected form of the data,  $\mathbf{f}$  is the distribution matrix  $\mathbf{F}$  stacked as a vector, and  $\mathbf{e}$  is an error vector. Although the marginal distributions  $h(a)$  and  $g(T_2)$  are independent, the two dimensions of the CPMG data both depend on  $t_e$ . Accordingly, the kernel function is non-separable and the matrix  $\mathbf{K}$  must be calculated in full, rather than as a Kronecker product (note that the standard 2D inversion of data assumes separable kernel functions<sup>44</sup>). To solve the problem efficiently, the size of the data matrix is reduced using a window averaging method described elsewhere.<sup>45</sup> This processing stage generates a diagonal precision matrix  $\mathbf{W}$  such that

$$\mathbf{W}^{1/2}\mathbf{b} = \mathbf{W}^{1/2}\mathbf{K}\mathbf{f} + \mathbf{e}. \quad (9)$$

The precision matrix accounts for changes in the apparent noise variance due to each window average. The size of the solution matrix  $\hat{\mathbf{F}}$  is also restricted. If both  $\mathbf{B}$  and  $\hat{\mathbf{F}}$  have dimensions  $32 \times 32$  then the optimization problem

$$\hat{\mathbf{f}} = \arg \min_{\mathbf{f} \geq 0} \|\mathbf{W}^{1/2}\mathbf{b} - \mathbf{W}^{1/2}\mathbf{K}\mathbf{f}\|^2, \quad (10)$$

can be solved on a desktop PC (e.g., 64-bit operating system running on a quad-core 3 GHz processor with 8 GB RAM) in a few seconds.

The optimization problem is further constrained by projecting the data onto a truncated singular value basis.<sup>46</sup> First the singular value decomposition (SVD) of the reduced kernel matrix is performed according to

$$\mathbf{USV}^T = \mathbf{W}^{1/2}\mathbf{K}, \quad (11)$$

where  $\mathbf{S}$  is a diagonal matrix of singular values,  $\mathbf{U}$  and  $\mathbf{V}$  are orthogonal singular basis matrices, and  $^T$  represents the transpose of a matrix. The number of singular values  $n_s$  is truncated to  $\tilde{n}_s$  based on the noise level of the data;  $\tilde{n}_s$  is determined as the largest number of singular values for which the smallest retained (i.e., the  $\tilde{n}_s$ th largest) singular value is greater than  $\sigma/b_{(1)}$ , where  $\sigma$  is the standard deviation of the noise and  $b_{(1)}$  is the first (largest) element in  $\mathbf{b}$ .<sup>43</sup> A matrix of significant singular values  $\tilde{\mathbf{S}}$  is obtained, and the basis matrices are truncated to  $\tilde{\mathbf{U}}$  and  $\tilde{\mathbf{V}}$  consistent with  $\tilde{\mathbf{S}}$ . The data vector is projected onto this compressed basis as  $\tilde{\mathbf{b}} = \tilde{\mathbf{U}}^T\mathbf{W}^{1/2}\mathbf{b}$ , which effectively filters the data to reduce the noise relative to the signal. Similarly, the compressed kernel matrix is  $\tilde{\mathbf{K}} = \tilde{\mathbf{S}}\tilde{\mathbf{V}}^T$ , and the optimization problem becomes

$$\hat{\mathbf{f}} = \arg \min_{\mathbf{f} \geq 0} \|\tilde{\mathbf{b}} - \tilde{\mathbf{K}}\mathbf{f}\|^2. \quad (12)$$

To solve Eq. (12) approximately we use Tikhonov regularization. This technique alleviates the ill-conditioning associated with matrix  $\tilde{\mathbf{K}}$  by adding a solution-roughness penalty term weighted by a smoothing parameter  $\alpha$  to modify the optimization problem in Eq. (12). The modified problem is

$$\hat{\mathbf{f}} = \arg \min_{\mathbf{f} \geq 0} \|\tilde{\mathbf{b}} - \tilde{\mathbf{K}}\mathbf{f}\|^2 + \alpha \|\mathbf{f}\|^2. \quad (13)$$

For a given  $\alpha$ , Eq. (13) is transformed with  $\mathbf{f} = \tilde{\mathbf{K}}^T\mathbf{c}$  where  $\mathbf{c}$  is a vector of fitting parameters given by  $\mathbf{c} = (\tilde{\mathbf{b}} - \tilde{\mathbf{K}}\mathbf{f})/\alpha$ .<sup>47</sup> The solution vector  $\hat{\mathbf{c}}$  is found by an unconstrained minimization. This solution vector is multiplied from the left by  $\tilde{\mathbf{K}}^T$  to determine  $\hat{\mathbf{f}}$ , which can be wrapped into the desired solution matrix  $\hat{\mathbf{F}}$ .<sup>44</sup> An optimum parameter  $\alpha_{\text{opt}}$  exists such that the best compromise is provided between smoothness and accuracy in the solution. Several methods are available for determining  $\alpha_{\text{opt}}$ ; GCV is fast and robust.<sup>43</sup> A GCV score  $\Phi$  is generated for a given  $\alpha$  as

$$\Phi(\alpha) = \frac{\tilde{n}_s \alpha^2 \|\hat{\mathbf{c}}\|^2}{(\tilde{n}_s - \hat{m}(\alpha))^2}, \quad (14)$$

where  $\hat{m}(\alpha)$  is the effective number of fitting parameters.<sup>48</sup> The value of  $\alpha$  is updated by recursion<sup>49</sup> until a minimum GCV score  $\Phi_{\text{opt}}$  is obtained, where  $\Phi_{\text{opt}} \equiv \Phi(\alpha_{\text{opt}})$ .

## A. The choice of $k$

The objective of generating an  $a$ - $T_2$  distribution is the determination of  $g(T_2)$ , i.e., a  $T_2$  distribution that depends only on surface relaxation. It is necessary to select the correct functional form of the diffusion exponent in the kernel matrix to separate the independent contributions to the signal decay and obtain a meaningful  $T_2$  distribution. Specifically, an appropriate power  $k$  defining the echo time dependence of the exponent must be selected. In general,  $k_{\text{opt}}$  is not known *a priori*. It is necessary, therefore, to repeat the inversion for a range of  $k$  values within the limit  $1 \leq k \leq 3$  to determine the appropriate diffusion exponent for the given data. Each inversion proceeds as described in Sec. III with the form of the kernel matrix determined by the choice of  $k$ .

To demonstrate the significance of selecting  $k_{\text{opt}}$  correctly, a simulated set of CPMG decays was projected from the simple Gaussian  $a$ - $T_2$  distribution shown in Fig. 2(a) using Eq. (9) with  $\mathbf{W}$  set to the identity matrix. The center of the Gaussian is located at  $T_2 = 1$  s,  $a = 10^3 \text{ s}^{-k}$ . This 2D Gaussian distribution is used as the basis for all simulated CPMG data through Secs. III A and IV B. First, the diffusion exponent for each decay was generated with a constant  $k_{\text{sim}} = 2$  (this notation is adopted to distinguish the power used to generate the simulated data from the  $k$  values tested during the fitting process, with  $k_{\text{opt}}$  corresponding to the best fit). Random noise, normally-distributed with zero mean, was added to provide a signal-to-noise ratio of  $\text{SNR} \approx 10^4$  (i.e., negligible noise). The simulated data containing  $32 \times 32$  values, shown in Fig. 2(b), were inverted to obtain  $\hat{\mathbf{F}}(T_2, a)$  for a selection of  $k$  values. The output distributions were limited to  $64 \times 64$  values with the  $T_2$  dimension bounded by  $\{10^{-2}, 10^2\}$  s and the  $a$  dimension bounded

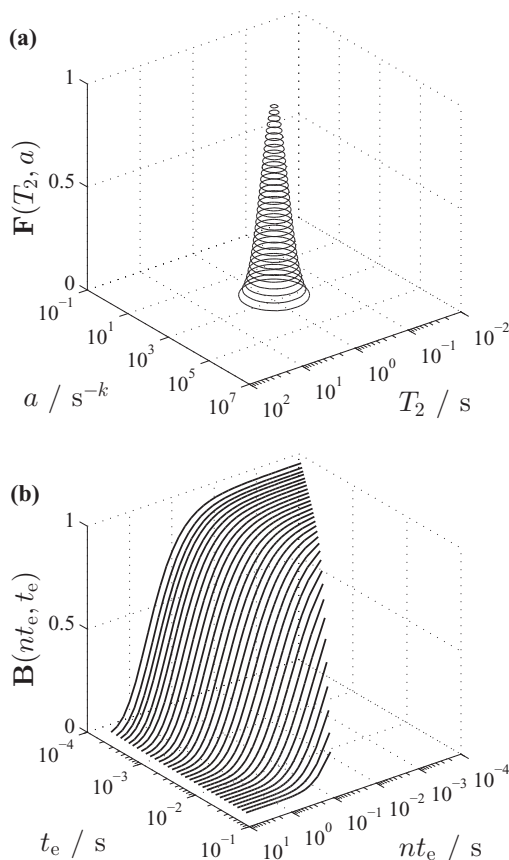


FIG. 2. Simulated CPMG data: (a) the ideal distribution  $F(T_2, a)$  is a 2D Gaussian. This distribution is used to generate CPMG data for a given  $k_{\text{sim}}$ . CPMG decays (b) with a diffusion exponent described by  $k_{\text{sim}} = 2$  were generated for 32 logarithmically spaced echo times ranging from  $t_e = 160 \mu\text{s}$  to 50 ms. The total number of echoes was varied to represent a constant acquisition time of 5 s.

by  $\{10^{-1}, 10^7\} \text{ s}^{-k}$ . Note that the numeric range of fitted  $a$  values (excluding units) does not change with the choice of  $k$ , although the units of  $a$  are determined by  $k$ .

The influence of  $k$  on the solution to the inverse problem is highlighted in Fig. 3. When the optimum value of  $k_{\text{opt}} = 2$  is selected, the resultant distribution  $\hat{F}(T_2, a)$  in Fig. 3(b) is a very close approximation to the original Gaussian distribution  $F(T_2, a)$  shown in Fig. 2(a). The 2D distribution in Fig. 3(b) is distorted slightly from the expected shape, suggesting insufficient smoothing has been applied, which might result from the combination of high SNR with lossy data compression. Despite this under-smoothing, the fitted marginal  $\hat{g}(T_2)$  plot is almost identical to the original Gaussian distribution. However, if the selected value of  $k$  is too small then the inversion shifts the distribution to artificially long  $T_2$  times and low  $a$  values, see Fig. 3(a). Conversely, if the selected value of  $k$  is too big then the inversion shifts the distribution to artificially short  $T_2$  times and large  $a$  values, see Fig. 3(c). In this latter situation, the distribution also becomes characteristically elongated in both the  $a$  and  $T_2$  dimensions. When an inappropriate value of  $k$  is selected, the fitted marginal  $\hat{g}(T_2)$  no longer resembles the original Gaussian distribution. Note that we have not included the marginal  $h(a)$  distributions in Fig. 3 because  $h(a)$  currently lacks a physical interpretation outside the limiting case of  $k = 3$ .

Note that the  $g(T_{2,\text{eff}})$  distribution is included in each marginal plot in Fig. 3. This distribution was obtained by inverting the simulated CPMG decay with the minimum echo time. The  $g(T_{2,\text{eff}})$  distribution is shifted to shorter relaxation times than the  $g(T_2)$  distribution in Fig. 3(b), indicating that the CPMG decay at  $t_e = 160 \mu\text{s}$  is not a valid approximation to the pure relaxation decay. This phenomenon is observed to some extent in all the  $g(T_{2,\text{eff}})$  distributions presented here, including those acquired from real samples in Sec. V.

Previously, the optimum diffusion exponent was determined by a manual search.<sup>26,27</sup> In this method, the value of  $k_{\text{opt}}$  was determined by looking for a data collapse in the diffusion contributions to the signal decay acquired with different echo times. The diffusive contribution is obtained by dividing each CPMG decay  $b(nt_e, t_e)$  by the pure relaxation contribution  $S(nt_e, 0)$ , such that

$$\begin{aligned} \frac{b(nt_e, t_e)}{S(nt_e, 0)} &= \frac{\int_{-\infty}^{\infty} \int_{-\infty}^{\infty} \exp\left\{-\frac{nt_e}{T_2} - ant_e^k\right\} f_k(T_2, a) d(\log_{10} T_2) d(\log_{10} a) + e(nt_e)}{\int_{-\infty}^{\infty} \exp\left\{-\frac{nt_e}{T_2}\right\} g(T_2) d(\log_{10} T_2)} \\ &= \int_{-\infty}^{\infty} \exp\left\{-ant_e^k\right\} h_k(a) d(\log_{10} a) + e^*(nt_e), \end{aligned} \quad (15)$$

where  $e^*$  is the scaled noise with non-uniform variance that varies with  $nt_e$ . The pure relaxation decay described by  $S(nt_e, 0)$  cannot be measured in practice. Ideally, it can be approximated with  $b(nt_e, t_e \rightarrow 0)$  using a CPMG decay obtained with the shortest echo time available on the NMR spectrometer.<sup>50</sup> However, depending on the hardware and the diffusion regime, this CPMG decay may not be a good approximation to  $S(nt_e, 0)$ .<sup>16</sup> The fitted CPMG signal  $\hat{S}(nt_e, 0)$  can instead be determined by taking the estimate of the

marginal distribution  $\hat{g}(T_2)$  from a given solution  $\hat{F}(T_2, a)$  and substituting into Eq. (3). This method is used to generate the data collapse plots in Sec. V. Note that  $\hat{S}(nt_e, 0)$  estimates  $S(nt_e, 0)$  only for  $k_{\text{opt}}$  and when the diffusion exponent is described exactly by a single value of  $k$  (see Secs. IV B and IV C for further discussions). Here we have the luxury of calculating  $S(nt_e, 0)$  exactly from the noise-free simulated distribution in Fig. 2(a). The normalized diffusive decay plots are shown in Fig. 4 where a data collapse is observed at

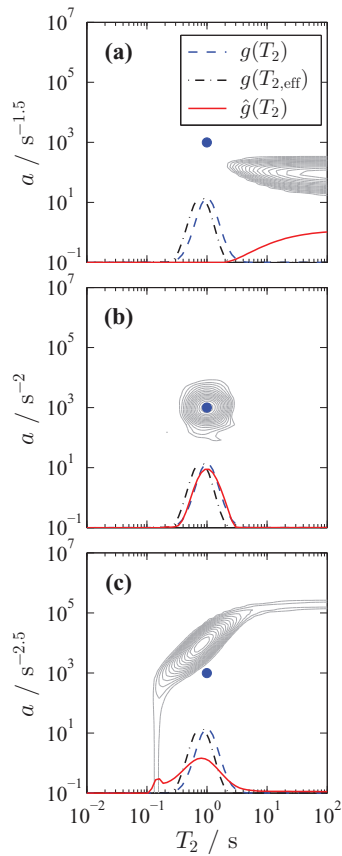


FIG. 3. Contour plots of  $\hat{\mathbf{F}}(T_2, a)$  obtained by inverting the simulated CPMG data ( $k_{\text{sim}} = 2$ ) in Fig. 2(b) with a diffusion exponent described by (a)  $k = 1.5$ , (b)  $k_{\text{opt}} = 2$ , and (c)  $k = 3$ . The contour intervals are the same in each plot. The center of the original 2D Gaussian distribution  $\mathbf{F}(T_2, a)$  is indicated in each plot by a solid blue dot. Included in each plot are the 1D marginal distributions  $\hat{g}(T_2)$  (solid red line) and  $g(T_2)$  (dashed blue line), see legend (applies to all plots). For completeness we also include the  $g(T_{2,\text{eff}})$  distribution (black dashed-dotted line) estimated by inverting the CPMG decay with  $t_e = 160 \mu\text{s}$ . The probability density scale is not shown for the marginal plots, but the distributions are normalized to unit area.

$k_{\text{opt}} = 2$  as expected. In this example the data collapse works perfectly. However, a complete collapse is rarely observed for real data, and the manual search for  $k_{\text{opt}}$  is inefficient. Therefore, we proceed to describe an automated search for  $k_{\text{opt}}$  that eliminates the variability of a manual search.

## B. Automated optimization of $k$

The GCV score described in Sec. III provides a metric of the quality of the fit to the data. This metric is sensitive to how well the assumed mathematical model represents the measured data. If the model used to define the kernel is varied and the optimization problem solved for a range of fitted functions, a minimum in  $\Phi_{\text{opt}}$  is obtained when the kernel matrix and measured data are most consistent. A similar quality factor can be obtained with  $\alpha_{\text{opt}}$ . When the kernel matrix and data are most consistent, less smoothing is required to obtain a stable solution, leading towards a minimum in  $\alpha_{\text{opt}}$ . In some cases, model selection can be achieved using a simpler criterion, minimizing the residual sum of squares. However, for the type of ill-posed regression problem being solved here, the

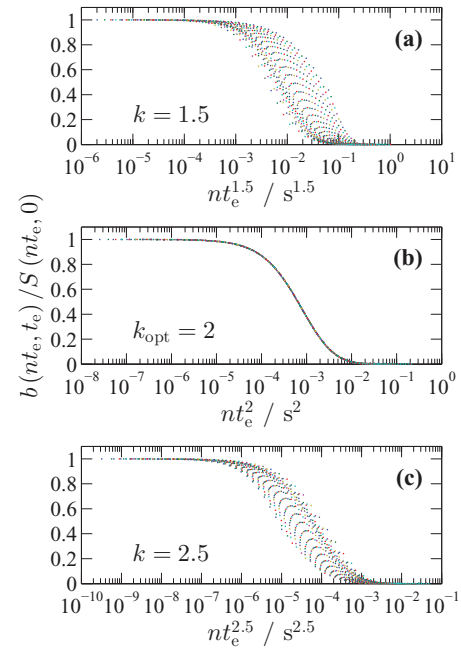


FIG. 4. Normalized diffusive decay plots obtained by applying Eq. (15) to the CPMG decays ( $k_{\text{sim}} = 2$ ) in Fig. 2(b) assuming (a)  $k = 1.5$ , (b)  $k_{\text{opt}} = 2$ , and (c)  $k = 3$ . Data collapse occurs for all  $nt_e^k$  only with  $k = k_{\text{opt}} = 2$ . Marker colors indicate different echo times from  $t_e = 0.16$  to  $50 \text{ ms}$ .

residual sum of squares does not provide a good comparator of different models.

The inversion of the CPMG data shown in Fig. 2(b) returns a GCV score corresponding to the optimum degree of smoothing for the chosen  $k$  value, according to Eq. (14). The variation in  $\Phi_{\text{opt}}(k)$  and  $\alpha_{\text{opt}}(k)$  are shown in Fig. 5 for the range  $1 \leq k \leq 3$ . A pronounced minimum is found in both  $\Phi_{\text{opt}}(k)$  and  $\alpha_{\text{opt}}(k)$  corresponding to  $k_{\text{opt}} = 2$  as expected.

The sensitivity in  $\Phi_{\text{opt}}(k)$  offers an unambiguous and quantitative metric for assessing the choice of  $k$ . Therefore, rather than explore the full range of  $k$  values,  $k_{\text{opt}}$  is located more accurately and efficiently by embedding the inversion algorithm in a search routine that performs a nonlinear minimization on  $\Phi_{\text{opt}}(k)$ . It is clear from Fig. 5 that both  $\Phi_{\text{opt}}$  and  $\alpha_{\text{opt}}$  are sensitive to the choice of  $k$ . However, the

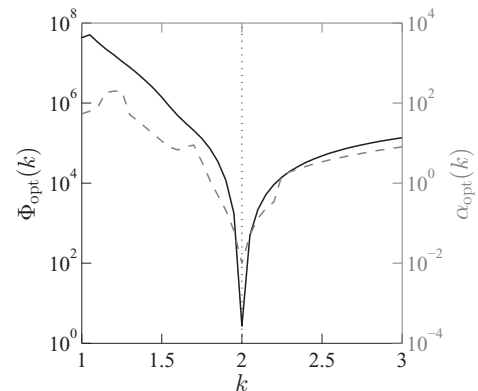


FIG. 5. Variation in  $\Phi_{\text{opt}}(k)$  and  $\alpha_{\text{opt}}(k)$  when inverting the simulated CPMG data in Fig. 2(b). The CPMG data were generated with  $k_{\text{sim}} = 2$  (dotted vertical line). A minimum occurs in both  $\Phi_{\text{opt}}(k)$  and  $\alpha_{\text{opt}}(k)$  at  $k_{\text{opt}} = 2$ .

variation in  $\Phi_{\text{opt}}(k)$  is smooth and continuous, making it more appropriate than  $\alpha_{\text{opt}}(k)$  for use in an automated minimization routine. A search performed on  $\alpha_{\text{opt}}$  is likely to return a false local minimum. It is important to note that a discontinuity exists in  $\Phi_{\text{opt}}(k)$  at  $k = 1$  exactly, because the contributions of  $T_2$  and the parameter  $a$  become indistinguishable in the kernel function. In this case, it is possible that a variety of  $a$ - $T_2$  distributions with similar smoothness penalty values can fit the measured data equally well with respect to the residual sum of squares. An artifact of this situation is that lower GCV scores can be achieved with  $k = 1$  than for cases with  $k$  slightly larger than unity. Therefore, when performing an automated minimization on  $\Phi_{\text{opt}}(k)$  it is important to restrict the search to  $1 < k \leq 3$ ;  $k = 1.1$  is an appropriate lower bound.

The minimum in  $\Phi_{\text{opt}}(k)$  is robust to the choice of  $k_{\text{sim}}$  used to generate the CPMG data. As long as  $k_{\text{sim}}$  is chosen within the expected range of  $1 \leq k \leq 3$ , the correct  $k_{\text{opt}}$  will be found. Even in the limiting cases of  $k_{\text{sim}} = 1$  or  $3$ , a minimum in  $\Phi_{\text{opt}}(k)$  will be present at the extreme end of the search range. Of course, in the special case of  $k_{\text{sim}} = 1$ , the resulting solution  $\hat{\mathbf{F}}(T_2, a)$  will not provide a meaningful  $T_2$  distribution. Bounded minimization routines tend to be inefficient at locating a minimum exactly at either the upper or lower bounds.<sup>51</sup> Therefore, if diffusion is expected in the ST asymptote the upper search bound may be increased to, say,  $k = 3.5$  to improve the efficiency of the minimization, although care must be taken in the interpretation if a value  $k_{\text{opt}} > 3$  is returned.

In general, the GCV score can be used to select a model for any variable within the kernel function. For example,  $T_1$  recovery is described by

$$\frac{S(t)}{S(0)} = 1 - C \exp \left\{ -\frac{t}{T_1} \right\}, \quad (16)$$

where the pre-exponent factor nominally takes the values  $C = 1$  (saturation recovery) and  $C = 2$  (inversion recovery).<sup>52</sup> It is often challenging to achieve complete inversion of the spin ensemble so that  $C < 2$  in practice. The actual degree of inversion depends on the quality of the radio frequency (rf) pulse ( $B_1$  homogeneity) and the pulse bandwidth relative to the width of the sample spectrum. The most appropriate value of  $C$  can be determined by searching for a minimum in  $\Phi_{\text{opt}}(C)$ . Another use in NMR could be the determination of a baseline offset on relaxation time measurements when only magnitude data are available.

#### IV. INVERSION QUALITY

In this section we consider parameters of the experiment and samples that influence the numeric inversion. These parameters generally prevent the ideal results illustrated in Sec. III from being observed in practice.

##### A. The effect of noise

Porous materials are often studied using low or intermediate field ( $B_0 \ll 1$  T) bench top magnets. Although SNR is not an inherent property of the instrument, it is common

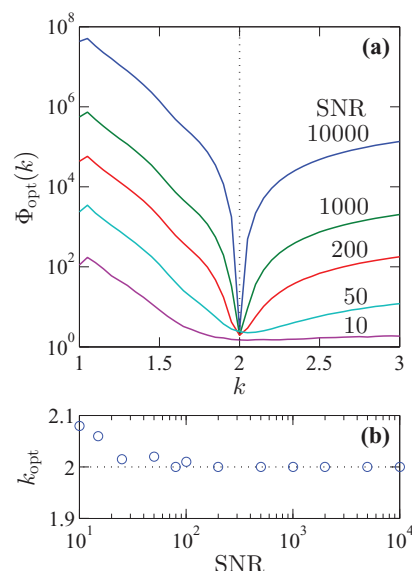


FIG. 6. Effect of noise on the determination of  $k_{\text{opt}}$ . The variation in  $\Phi_{\text{opt}}(k)$  is shown in (a) when inverting simulated CPMG data with added noise. The CPMG data were generated with  $k_{\text{sim}} = 2$  (dotted vertical line) in all cases. The series of  $\Phi_{\text{opt}}(k)$  plots (top to bottom) correspond to CPMG data generated with decreasing SNR; the top (blue) line is repeated from Fig. 5. The variation in  $k_{\text{opt}}$  is shown as a function of SNR in (b); these values were obtained by performing a nonlinear minimization of  $\Phi_{\text{opt}}(k)$  as described in Sec. III B.

for such systems to deliver a relatively poor SNR,<sup>5</sup> especially when studying low porosity samples. Therefore, it is important to understand the influence of noise on the determination of  $k_{\text{opt}}$  and the minimum SNR required for a reliable minimization of  $\Phi_{\text{opt}}(k)$ . The variation in  $\Phi_{\text{opt}}(k)$  observed when inverting simulated CPMG data generated at various SNR is shown in Fig. 6(a). As the noise level increases,  $\Phi_{\text{opt}}$  decreases for a given  $k$ . Furthermore,  $\Phi_{\text{opt}}(k)$  becomes less sensitive to changes in  $k$  as the noise increases. In the extreme example of  $\text{SNR} = 10$ , the dip in  $\Phi_{\text{opt}}(k)$  around  $k_{\text{opt}}$  is broad and shallow, rather than the well-defined minimum observed at higher SNR. This behavior is typical of GCV.<sup>53</sup> Notwithstanding, it is possible to obtain a reasonable estimate of  $k_{\text{opt}}$  down to low SNR, see Fig. 6(b). The correct value of  $k_{\text{opt}} = 2$  is obtained for  $\text{SNR} > 200$ , consistent with other minimum SNR estimates (i.e.,  $\text{SNR} > 100$ ) required for robust interpretation of 2D NMR measurements.<sup>21,54</sup>

##### B. The effect of echo time

The regime governing diffusion in a porous material depends on the length  $\ell_e$ , see Fig. 1, which is in turn determined by the experimental echo time. For a single CPMG decay, we know  $\ell_e$  and hence can predict the relevant diffusion behavior; examples are to be found in the literature.<sup>16,26,27</sup> However, the generation of an  $a$ - $T_2$  distribution requires CPMG data to be acquired with a range of echo times. If one is fortunate, all the echo times will fall within an asymptotic diffusion regime (specifically the ST regime). More likely, an increase in two orders of magnitude in  $t_e$  will result in an increase in  $\ell_e/\ell_s$  of over an order of magnitude (recalling that  $\ell_e \propto \sqrt{T_e}$ ). This change in  $t_e$  is equivalent to moving horizontally from left to



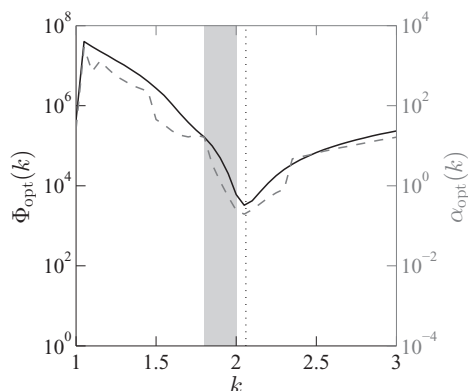


FIG. 7. Variation in  $\Phi_{\text{opt}}(k)$  and  $\alpha_{\text{opt}}(k)$  when inverting simulated CPMG data. The CPMG data were generated with variable  $k_{\text{sim}} = 2 \rightarrow 1.8$  (gray rectangle). The minimum in  $\Phi_{\text{opt}}(k)$  occurs at  $k_{\text{opt}} = 2.06$  (dotted vertical line).

right across the plot in Fig. 1. Therefore, while the diffusive contribution to the CPMG decay acquired with the shortest echo time might obey the ST asymptote, data acquired with longer echo times could depend on some pre-asymptotic diffusion regime.

To simulate a change in  $\ell_e$  with  $t_e$  that influences the diffusion behavior, CPMG data were generated from the distribution in Fig. 2(a) such that  $k_{\text{sim}}$  varied with  $t_e$ , while  $\text{SNR} = 10^4$ . As the echo time increased logarithmically from  $t_e = 160 \mu\text{s}$  to 50 ms, the diffusion exponent was adjusted by linearly decreasing  $k_{\text{sim}}$  over the interval  $k_{\text{sim}} = 2 \rightarrow 1.8$ . Although the dependence of  $k$  on  $\ell_e/\ell_s$  is presently unknown, we consider this range of  $k$  to be a representative model for the range of length scale ratios  $\ell_e/\ell_s = 1 \rightarrow 20$  based on our previous empirical studies.<sup>26,27</sup>

A plot of  $\Phi_{\text{opt}}(k)$  for the inversion of these data is shown in Fig. 7. A minimum in GCV score is found at  $k_{\text{opt}} = 2.06$ , slightly higher than any of the  $k_{\text{sim}}$  values used to generate the CPMG decays.

Data collapse plots for these CPMG data are shown in Fig. 8. Given the form of the decays, a perfect data collapse cannot be obtained. Even at  $k_{\text{opt}} = 2.06$ , there is some deviation between the normalized diffusive decay curves. The solution  $\hat{\mathbf{F}}(T_2, a)$  obtained at  $k_{\text{opt}}$ , see Fig. 9, is a reasonable approximation to the original 2D Gaussian distribution given the non-uniform diffusive distortion in the CPMG decays. Importantly, the projected marginal distribution  $\hat{g}(T_2)$  is similar to the true distribution with the modal amplitude at  $T_2 = 1$  s as expected.

The difference between the data collapse plot at  $k_{\text{opt}} = 2.06$ , Fig. 8(c), and  $k = 2$ , Fig. 8(b), is small. If performing a manual search for  $k_{\text{opt}}$ , it is likely that  $k = 2$  would be considered to give the closest approximation to a data collapse, and this would be a satisfactory choice. It is interesting to note that, in this example, the data collapse fails as  $k$  is reduced, cf. Figs. 8(c) and 8(a). This result is counter-intuitive as one may expect  $k_{\text{opt}}$  to obey  $2 \geq k_{\text{opt}} \geq 1.8$  based on the range of  $k_{\text{sim}}$  used to generate the CPMG data. Other similar situations have been simulated (results not shown): for example, if CPMG data are generated with  $k_{\text{sim}} = 2 \rightarrow 1.5$ , then  $k_{\text{opt}} \approx 2.3$ . In the

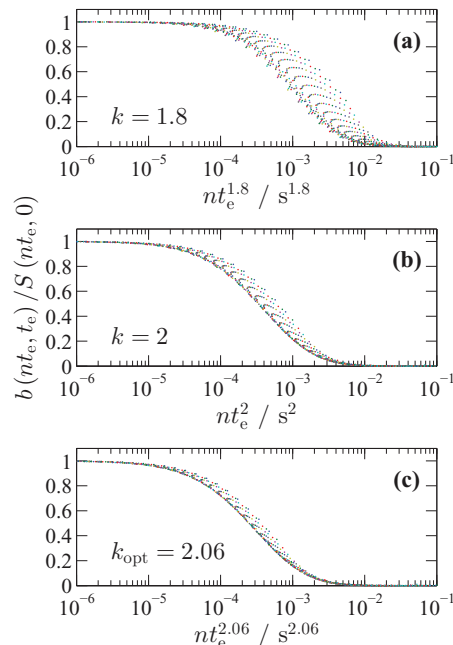


FIG. 8. Normalized diffusive decay plots obtained by applying Eq. (15) to simulated CPMG decays ( $k_{\text{sim}} = 2 \rightarrow 1.8$ ) assuming a diffusion exponent described by (a)  $k = 1.8$ , (b)  $k = 2$ , and (c)  $k_{\text{opt}} = 2.06$ . Marker colors indicate different echo times from  $t_e = 0.16$  to 50 ms.

extreme limit that  $k_{\text{sim}}$  varies by much more than 0.5, e.g.,  $k_{\text{sim}} = 2 \rightarrow 1.2$ , we find  $k_{\text{opt}} > 3$ . For such unexpected values of  $k_{\text{opt}}$  it is difficult to consider the  $T_2$  marginal distribution from the corresponding solution  $\hat{\mathbf{F}}(T_2, a)$  as meaningful. Any result in which  $k > 3$  should be considered an artifact of the experimental conditions. However, this observation that  $k_{\text{opt}} > k_{\text{sim}}$  is not universal. For example, if CPMG decays are generated with  $k_{\text{sim}} = 3 \rightarrow 2.5$ , then  $k_{\text{opt}} \approx 2.8$ . When inverting real data, it is important to check the quality of the data collapse and solution obtained at  $k_{\text{opt}}$  to assess whether the inversion is sensible.

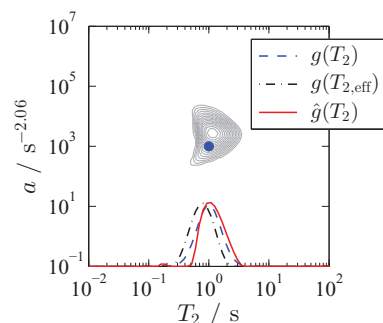


FIG. 9. Contour plot of  $\hat{\mathbf{F}}(T_2, a)$  obtained by inverting simulated CPMG decays ( $k_{\text{sim}} = 2 \rightarrow 1.8$ ) with a diffusion exponent described by  $k_{\text{opt}} = 2.06$ . The center of the original 2D Gaussian distribution  $\mathbf{F}(T_2, a)$  is indicated by the solid blue dot. Included are the 1D marginal distributions  $\hat{g}(T_2)$  (solid red line) and  $g(T_2)$  (dashed blue line), see legend. For completeness we also include the  $g(T_{2,\text{eff}})$  distribution (black dashed-dotted line) estimated by inverting the CPMG decay with  $t_e = 160 \mu\text{s}$ . The probability density scale is not shown for the marginal plots, but the distributions are normalized to unit area.

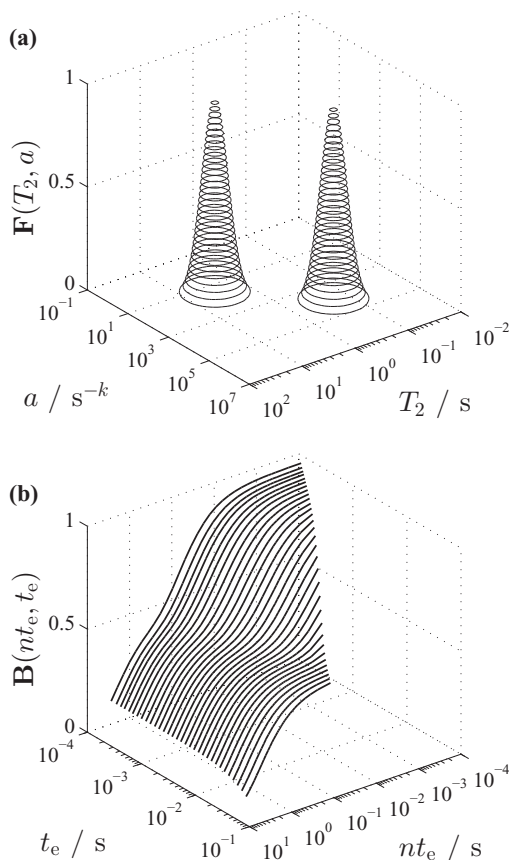


FIG. 10. Simulated CPMG data: (a) the ideal distribution  $F(T_2, a)$  is a bimodal 2D Gaussian. This distribution is used to calculate CPMG decays (b) with a diffusion exponent described by  $k_{\text{sim}} = 2$  (short  $T_2$ , large  $a$ ) or  $k_{\text{sim}} = 3$  (long  $T_2$ , small  $a$ ). The CPMG data were generated for 32 logarithmically spaced echo times ranging from  $t_e = 160 \mu\text{s}$  to 50 ms. The total number of echoes was varied to represent a constant acquisition time of 5 s.

### C. Heterogeneous systems

So far we have considered examples of systems with a single mean  $T_2$  relaxation time. However, many real materials exhibit multi-modal  $T_2$  distributions. Packed beds of porous particles, such as those found in heterogeneous catalytic reactors, will have a bimodal  $T_2$  distribution corresponding to inter- and intra-granular porosity.<sup>55</sup> Similarly, carbonate rocks often exhibit macropores (dissolution vugs) and micropores (“matrix” porosity) characterized by long and short  $T_2$  relaxation times, respectively.<sup>34</sup> Cementitious materials can have multi-modal  $T_2$  distributions corresponding to structures spanning a hierarchy of length scales.<sup>56,57</sup> It is likely that diffusion occurring in pores of different size will be governed by different regimes due to the variation in  $\ell_s$ . We emulate diffusion and relaxation in a structure with two characteristic pore sizes using the distribution in Fig. 10(a). The two Gaussian distributions are centered at  $T_2 = 4.6$  s,  $a = 46 \text{ s}^{-k}$  (macropores) and  $T_2 = 0.22$  s,  $a = 22000 \text{ s}^{-k}$  (micropores). The CPMG data in Fig. 10(b) were generated using  $k_{\text{sim}} = 3$  (macropores) and  $k_{\text{sim}} = 2$  (micropores), equivalent to at least an order of magnitude difference in  $\ell_s$  between the two modal pore sizes according to Fig. 1. For this example, a SNR =  $10^4$  was retained.

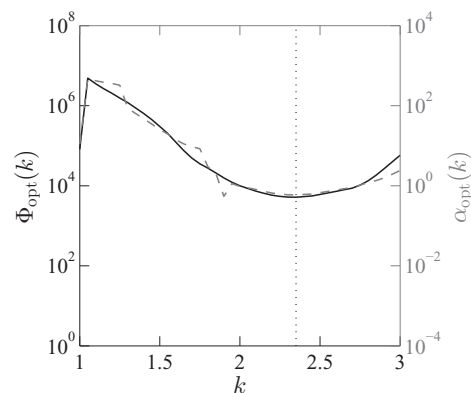


FIG. 11. Variation in  $\Phi_{\text{opt}}(k)$  and  $\alpha_{\text{opt}}(k)$  when inverting the simulated CPMG data ( $k_{\text{sim}} = 2, 3$ ) in Fig. 10(b). The minimum in  $\Phi_{\text{opt}}(k)$  occurs at  $k_{\text{opt}} = 2.35$  (dotted vertical line).

The minimum obtained in  $\Phi_{\text{opt}}(k)$  when inverting the CPMG data from Fig. 10(b) is shallow and broad; see Fig. 11. There is only a weak  $k$  dependence in  $\Phi_{\text{opt}}(k)$  on the  $\log_{10}$  scale over the range  $2.1 \leq k \leq 2.5$ , suggesting little difference in the quality of the fit to the data for these  $k$  values. Here,  $\alpha_{\text{opt}}(k)$  is a worse metric: a false minimum exists around  $k \approx 1.9$  even at this high SNR. Nevertheless, by minimizing  $\Phi_{\text{opt}}(k)$  we determine  $k_{\text{opt}} = 2.35$  for these data.

It is interesting to see that, for a bimodal distribution, the data collapse plots in Fig. 12 offer no useful indication of  $k_{\text{opt}}$ . Over the range  $2 \leq k \leq 3$  it is almost impossible to determine which set of normalized diffusive decays most closely approximates a data collapse. On close inspection of the plots in Fig. 12, it appears a best approximation to a data collapse occurs at  $k = 2$ , but only for times  $nt_e^2 < 10^{-5} \text{ s}^2$ .

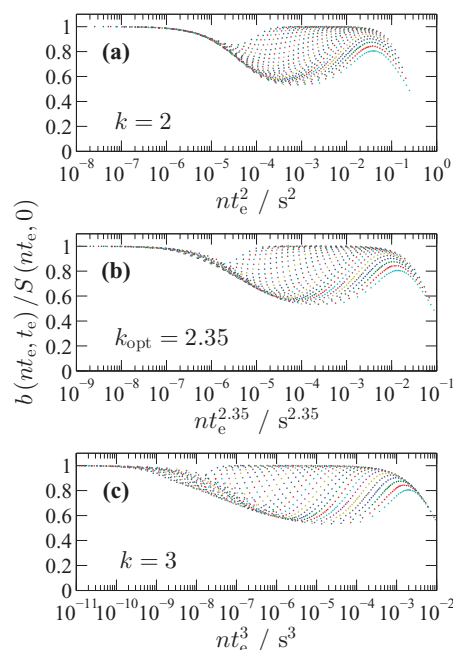


FIG. 12. Normalized diffusive decay plots obtained by applying Eq. (15) to the CPMG data ( $k_{\text{sim}} = 2, 3$ ) in Fig. 10(b) assuming a diffusion exponent described by (a)  $k = 2$ , (b)  $k_{\text{opt}} = 2.35$ , and (c)  $k = 3$ . Marker colors indicate different echo times from  $t_e = 0.16$  to 50 ms.

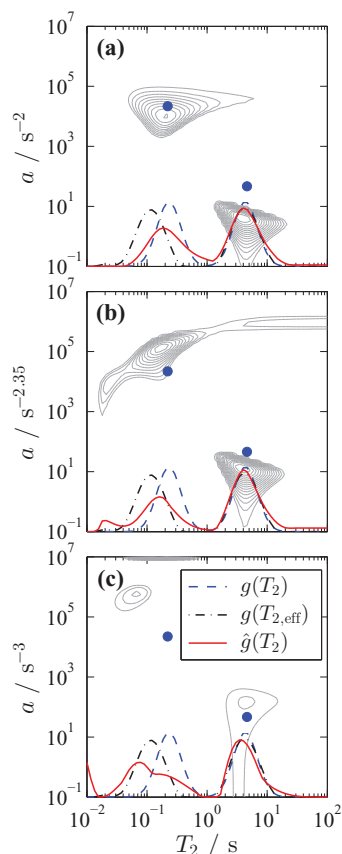


FIG. 13. Contour plots of  $\hat{\mathbf{F}}(T_2, a)$  obtained by inverting the simulated CPMG decays ( $k_{\text{sim}} = 2, 3$ ) in Fig. 10(b) with a diffusion exponent described by (a)  $k = 2$ , (b)  $k_{\text{opt}} = 2.35$ , and (c)  $k = 3$ . The two modal positions of the original distribution  $\mathbf{F}(T_2, a)$  are indicated in each plot by the solid blue dots. Included in each plot are the 1D marginal distributions  $\hat{g}(T_2)$  (solid red line) and  $g(T_2)$  (dashed blue line), see legend (applies to all plots). For completeness we also include the  $g(T_{2,\text{eff}})$  distribution (black dashed-dotted line) estimated by inverting the CPMG decay with  $t_e = 160 \mu\text{s}$ . The probability density scale is not shown for the marginal plots, but the distributions are normalized to unit area.

Regardless of the choice of  $k$ , the diffusive decays diverge once  $nt_e^k > 10^{-3k} \text{ s}^k$ . This observation suggests the data collapse method for determining  $k_{\text{opt}}$  is unhelpful in heterogeneous materials. Of course, the data collapse will work for media with bimodal pore size distributions if all diffusion occurs in the same regime, as demonstrated in the seminal work of Hürlimann.<sup>50</sup> In general, though,  $k_{\text{opt}}$  should be determined by minimizing  $\Phi_{\text{opt}}(k)$ .

Here, the choice of  $k$  has a significant impact on the solution  $\hat{\mathbf{F}}(T_2, a)$ . If we assume  $k = 2$ , then the inversion algorithm recovers the peak at short  $T_2$ , large  $a$  (encoded with  $k_{\text{sim}} = 2$ ) as expected, see Fig. 13(a). Alternatively, if we assume  $k = 3$ , then the inversion algorithm instead recovers the peak at long  $T_2$ , small  $a$  (encoded with  $k_{\text{sim}} = 3$ ), see Fig. 13(c). However, in this case a significant proportion of the intensity in the output distribution is located at the lower bound of  $T_2 = 10^{-2} \text{ s}$  and upper bound of  $a = 10^7 \text{ s}^{-3}$ . A compromise between these two extremes is found with  $k_{\text{opt}} = 2.35$ , see Fig. 13(b). The peak at short  $T_2$ , large  $a$  (encoded with  $k_{\text{sim}} = 2$ ) is artificially stretched along the  $T_2$  dimension, consistent with an over-estimate of  $k$ , cf. Figs. 13(b) and

3(c). The peak at long  $T_2$ , small  $a$  (encoded with  $k_{\text{sim}} = 3$ ) is also distorted, but less so. It is interesting to note that the marginal distribution  $\hat{g}(T_2)$  obtained with  $k = 2$  is the closest approximation for the original bimodal  $T_2$  distribution. The  $T_2$  distribution obtained assuming  $k = 3$  is a poor approximation to the original. When analyzing this type of data for real samples, it is advisable to obtain  $k_{\text{opt}}$  by minimizing  $\Phi_{\text{opt}}(k)$  and then consider solutions  $\hat{\mathbf{F}}(T_2, a)$  for  $k$  values near to  $k_{\text{opt}}$  to obtain a sensible  $a$ - $T_2$  distribution that is free from obvious distortions. The  $T_2$  distribution obtained with  $k_{\text{opt}} = 2.35$  provides a reasonable estimate for the true bimodal distribution. Care is required to correctly interpret the distortion at short  $T_2$  times as an artifact of the inversion process.

By considering a series of CPMG data sets, we have demonstrated that the quality of the  $a$ - $T_2$  distribution is dependent on the SNR of the data and also properties of the acquisition protocol and sample. Although we have attempted to simulate situations that could arise in real samples, the data were all ideal. In practice, the quality of CPMG data can be influenced by details of the experiment, hardware, and processing. Often the minimum echo time used is dictated by the maximum rf duty cycle of the probe and amplifier. However, it is also possible to lock the spin ensemble to the  $B_1$  field if the rf duty cycle is too high, resulting in artificially slow relaxation at short echo times.<sup>58</sup> As a rule of thumb, the minimum echo time should be selected such that  $t_e \geq T_2^*$ , where  $T_2^*$  is the transverse relaxation due to local field inhomogeneities. Conversely, there may be particular echo times that produce artificially fast relaxation: typically when  $t_e$  is equal to the inverse of the mains electricity frequency (or harmonics thereof) such that oscillations in  $B_0$  sum coherently along the echo train. This effect is caused by environmental interference and, though uncommon, has been encountered on permanent magnets.<sup>5</sup> Furthermore, careful data processing is required to ensure precise phase rotation of the real and quadrature channels, and to remove any baseline offset. Overall, it is important to check the quality of the raw data prior to applying the inversion methods described here: CPMG data should always be smooth, continuous, and decrease monotonically as  $t_e$  increases.

## V. EXAMPLES

In this section we apply our optimized inversion method described in Sec. III to a series of real materials. We use these examples to demonstrate the experimental manifestation of the conditions simulated in Sec. IV.

### A. Glass beads

A packed bed of non-porous borosilicate glass beads, saturated with water, was measured at  $B_0 = 2 \text{ T}$  ( $\nu_0 = 85 \text{ MHz}$  for  $^1\text{H}$ ). Relaxation and diffusion in this system has been considered previously.<sup>27,38</sup> CPMG decays were obtained with echo times ranging from  $t_e = 2$  to  $20 \text{ ms}$  in 32 logarithmically spaced increments, and a SNR  $\sim 2000$ . The minimum echo time was limited by the duty cycle of the rf probe. Typical rf pulse durations were  $t_{90} = 15 \mu\text{s}$  and  $t_{180} = 30 \mu\text{s}$  for the  $90^\circ$

and  $180^\circ$  tip angles, respectively. The borosilicate beads had a nominal diameter of  $100\ \mu\text{m}$ . The glass was diamagnetic and exhibited a susceptibility contrast of  $\Delta\chi = 5.5 \times 10^{-6}$  against water, measured using a Sherwood Scientific [Cambridge, UK] Mk1 Susceptibility Balance.

The diffusion behavior expected to be observed when measuring the water in this system is assessed by estimating the ratios  $\ell_e/\ell_s$  and  $\ell_g/\ell_s$ . For the given range of echo times,  $\ell_e$  ranged from  $2.5$  to  $6.5\ \mu\text{m}$ . Defining the relevant characteristic pore size  $\ell_s$  describing the interstices between the glass spheres is non-trivial. We have taken the maximum distance between the glass beads as  $30\ \mu\text{m}$  (estimated using optical microscopy) and the minimum distance as an order of magnitude smaller, at  $3\ \mu\text{m}$  (equivalent to the shortest diffusion path). Calculating a reasonable range of  $\ell_g$  lengths is even less straight-forward: an estimate of  $g_{\text{eff}}$  is required. An upper limit on the effective gradient  $g_{\text{max}}$  can only be obtained by assuming features of the ST asymptote,<sup>50</sup> such that

$$g_{\text{max}} \approx \left(\frac{\gamma}{D}\right)^{1/2} (\Delta\chi B_0)^{3/2}. \quad (17)$$

For the water-saturated bead pack,  $g_{\text{max}} \approx 12\ \text{T m}^{-1}$ , taking the free diffusion coefficient of water as  $D = 2.3 \times 10^{-9}\ \text{m}^2\ \text{s}^{-1}$  ( $25^\circ\text{C}$ ). The minimum effective gradient is expected to be an order of magnitude lower than  $g_{\text{max}}$ , based on previous studies.<sup>38</sup> Accordingly, we estimate  $\ell_g$  as ranging from  $6$  to  $10\ \mu\text{m}$ , acknowledging that if diffusion occurs outside the ST asymptote, the true  $\ell_g$  may be significantly smaller. We note, however, that outside the ST asymptote, the maximum effective gradient will be smaller than  $g_{\text{max}}$  estimated using Eq. (17), as described elsewhere,<sup>38</sup> so we assume the  $g_{\text{eff}}$  values calculated by this method remain relevant. The range of diffusion behaviors that are expected to be applicable to this sample are shown in Fig. 14. Based on our estimates of  $\ell_e/\ell_s$  and  $\ell_g/\ell_s$ , we expect the diffusion behavior to be governed by the pre-asymptotic ST regime.

Previously, we estimated  $k_{\text{opt}} \approx 2.2$  for these water-saturated glass beads, based on the near-equivalence of the three length scales and a manual search for  $k_{\text{opt}}$  using data collapse plots.<sup>27</sup> In the present work we perform a minimization

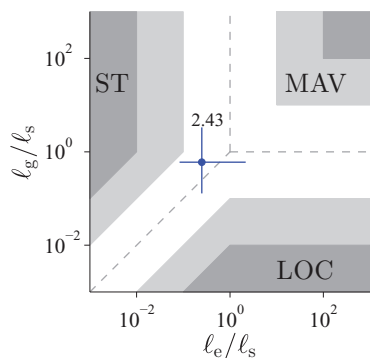


FIG. 14. Schematic illustrating the diffusion regimes ST, MAV, and LOC as defined by the length scales  $\ell_e$ ,  $\ell_s$ , and  $\ell_g$ . The expected diffusion behavior of water in a packed bed of non-porous borosilicate glass spheres is shown by the blue dot. The solid blue lines indicate the maximum expected range of valid diffusion behaviors based on estimates of the diffusion length scales, as described in the text. The value of  $k_{\text{opt}} = 2.43$ , obtained by minimization of the GCV score (see Fig. 15), is noted on the plot.

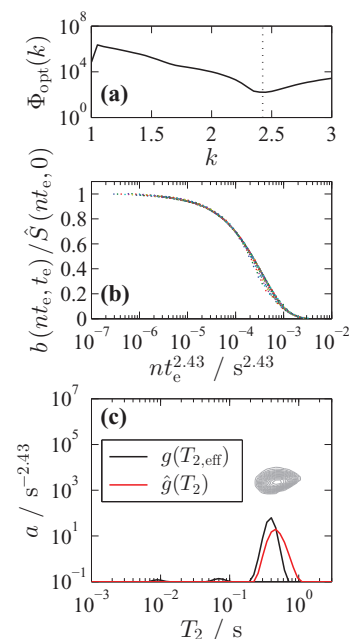


FIG. 15. Process of obtaining the  $T_2$  distribution for a water-saturated glass bead pack. The optimum power in the diffusion exponent  $k_{\text{opt}} = 2.43$  is obtained by minimizing the GCV score; a plot of  $\Phi_{\text{opt}}(k)$  is shown in (a). The choice of  $k_{\text{opt}}$  is confirmed by the data collapse plot in (b). Marker colors indicate different echo times from  $t_e = 2$  to  $20\ \text{ms}$ . An  $a$ - $T_2$  distribution (c) is generated at  $k_{\text{opt}}$  and the marginal distribution  $\hat{g}(T_2)$  (solid red line) is projected from the 2D plot, see legend. For comparison, the estimated  $g(T_{2,\text{eff}})$  distribution (solid black line) is included, calculated from the CPMG decay with the minimum  $t_e = 2\ \text{ms}$ . The probability density scale is not shown for the marginal plots, but the distributions are normalized to unit area.

on the GCV score to obtain  $k_{\text{opt}} = 2.43$ , see Fig. 15(a) where a distinct minimum is obtained in the plot of  $\Phi_{\text{opt}}(k)$ . The data collapse (Fig. 15(b)) obtained at this  $k_{\text{opt}}$  is excellent, which suggests that the entire spin ensemble experiences a common regime for diffusion in the presence of a non-uniform magnetic field. For experimental data we do not know, *a priori*, the underlying  $T_2$  decay rate which was available in the simulated data discussed in Sec. IV. Here, then, we generate the data collapse plot by normalizing the CPMG decays with the expected signal decay  $\hat{S}(nt_e, 0)$  calculated using  $\hat{g}(T_2)$  obtained from  $\hat{\mathbf{F}}(T_2, a)$  at  $k_{\text{opt}}$ , see Fig. 15(c). The  $a$ - $T_2$  distribution for the water-saturated bead pack is monomodal and approximately Gaussian, with no strong correlation between  $a$  and  $T_2$  as expected. Our focus is on the projected  $\hat{g}(T_2)$  marginal distribution as the distribution in  $a$  lacks a physical interpretation at present. The “true”  $T_2$  distribution is monomodal with a log-mean  $T_{2\text{lm}} = 0.46\ \text{s}$  (the log-mean relaxation time is the mean value determined on the  $\log_{10}$  scale), and spans less than an order of magnitude in  $T_2$ . In contrast, the  $T_{2,\text{eff}}$  distribution, obtained from the CPMG decay with  $t_e = 2\ \text{ms}$  (minimum echo time), is multimodal with several low-amplitude components at short  $T_2$  times, and the modal relaxation time of the main peak occurs at  $T_{2,\text{eff}} = 0.2\ \text{s}$ .

Given the SNR of the experimental data, the results achieved in Fig. 15 bear close resemblance to the simulated results illustrated in Figs. 3–5. The water-saturated glass bead pack is an example of a homogeneous sample, wherein ideal diffusion behavior is expected, albeit outside the asymptotic



TABLE I. Properties of porous ceramic cylinders saturated with low-salinity brine.

Sample	Pore size/ $\mu\text{m}$	Porosity	$\Delta\chi$	$\ell_g/\mu\text{m}$	$k_{\text{opt}}$
DP81-82	0.3 $\rightarrow$ 2	0.37	$8.06 \times 10^{-5}$	0.6 $\rightarrow$ 2.8	2.42
DP215	10 $\rightarrow$ 20	0.40	$9.99 \times 10^{-5}$	0.5 $\rightarrow$ 2.5	2.68
DP36g	50 $\rightarrow$ 60	0.44	$1.86 \times 10^{-4}$	0.4 $\rightarrow$ 1.8	2.78
DP28	60 $\rightarrow$ 120	0.34	$1.76 \times 10^{-5}$	1.3 $\rightarrow$ 5.9	2.57

limit of the ST regime. The quality of the data collapse and  $T_2$  distribution shown in Fig. 15 validate our automated method for determining  $k_{\text{opt}}$  in a real system.

## B. Porous ceramics

Four porous cylinders of sintered alumina beads (ceramic) were supplied by HP Technical Ceramics [Sheffield, UK] with external dimensions 50 mm  $\times$  38 mm (length  $\times$  diameter). These ceramics are designed as filters, so are available with different pore sizes. The properties of the four samples are listed in Table I; the pore sizes given in the table are quoted from the manufacturer. The alumina is held together by a binder which contains iron oxide, leading to relatively large magnetic susceptibilities,<sup>59</sup> especially in sample DP36g which had a visible red coloration due to the high iron oxide content. The ceramic cylinders were vacuum saturated with a low-salinity brine (total dissolved solids, TDS = 4800 ppm, predominantly sodium chloride and sodium hydrogen carbonate). The susceptibility contrast between the ceramics and brine are given in Table I, measured using a Bartington Instruments [Witney, Oxon, UK] MS2C sensor. The corresponding estimated ranges of  $\ell_g$  at  $B_0 = 0.3$  T ( $\nu_0 = 12.9$  MHz for  $^1\text{H}$ ) are included in Table I, although we again note that these dephasing lengths are obtained by assuming features of the ST regime.

CPMG data were acquired from the ceramic samples with echo times ranging from  $t_e = 160$   $\mu\text{s}$  to 20 ms in 32 logarithmically spaced increments. These echo times lead to diffusion path lengths ranging from  $\ell_e = 0.43$  to 7.58  $\mu\text{m}$ . The data had a SNR  $\sim 5000$ . The expected diffusion behavior of the brine-saturated ceramics is shown in Fig. 16. At the shortest echo time, all the samples are expected to exhibit diffusion behavior consistent with the pre-asymptotic ST regime. The diffusive contribution to the CPMG decay for water in sample DP28, having the largest pores and lowest susceptibility contrast, will be governed by the ST asymptote at the shortest echo time. However, due to the wide range of echo times explored in these measurements, we can expect to observe diffusion governed by another regime as  $t_e$  increases. For samples DP215, DP36g, and DP28, the pre-asymptotic LOC regime becomes relevant at long echo times. For DP81-82, the pre-asymptotic MAV regime becomes relevant at long echo times because of the small pore size in this sample.

We now consider the determination of  $\hat{g}(T_2)$  for DP215 as a typical example. A minimization performed on the GCV score provides  $k_{\text{opt}} = 2.68$ , see Fig. 17(a). In this case, a distinct minimum is not observed in the plot of  $\Phi_{\text{opt}}(k)$ . It is dif-

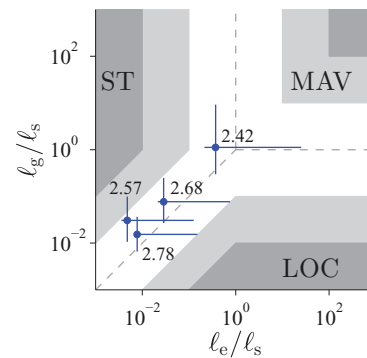


FIG. 16. Schematic illustrating the diffusion regimes ST, MAV, and LOC as defined by the length scales  $\ell_e$ ,  $\ell_s$ , and  $\ell_g$ . The expected diffusion behaviors of low-salinity brine in porous ceramics are shown by the blue dots. The solid blue lines indicate the maximum expected range of valid diffusion behaviors based on estimates of the diffusion length scales. The values of  $k_{\text{opt}}$ , obtained by minimization of the GCV score (see Table I), are noted on the plot for each sample.

ficult to distinguish the difference in  $\Phi_{\text{opt}}(k)$  on the  $\log_{10}$  scale between  $k = 2.3$  to 2.8. The data collapse is not helpful in this example either, see Fig. 17(b). Even at  $k_{\text{opt}}$ , the normalized decay curves diverge and the data collapse breaks down. The shallow minimum in  $\Phi_{\text{opt}}(k)$  and failure of the data collapse observed here is entirely consistent with the simulated results shown in Figs. 7 and 9. The wide range of echo times used in the data acquisition has resulted in a non-unique power

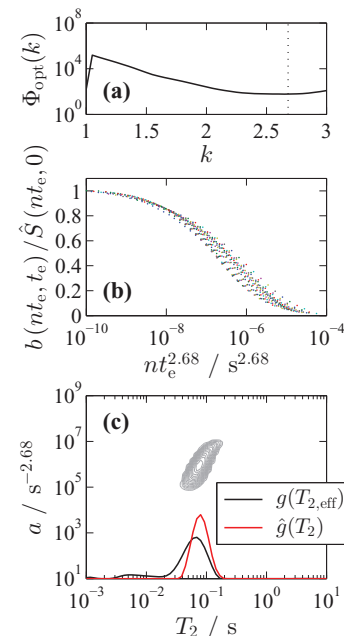


FIG. 17. Process of obtaining the  $T_2$  distribution for the brine-saturated DP215 porous ceramic. The optimum power in the diffusion exponent  $k_{\text{opt}} = 2.68$  is obtained by minimizing the GCV score; a plot of  $\Phi_{\text{opt}}(k)$  is shown in (a). The choice of  $k_{\text{opt}}$  is supported by the data collapse plot in (b). Marker colors indicate different echo times from  $t_e = 0.16$  to 20 ms. An  $a$ - $T_2$  distribution (c) is generated at  $k_{\text{opt}}$  and the marginal distribution  $\hat{g}(T_2)$  (solid red line) is projected from the 2D plot, see legend. For comparison, the estimated  $g(T_{2,\text{eff}})$  distribution (solid black line) is included, calculated from the CPMG decay with the minimum  $t_e = 160$   $\mu\text{s}$ . The probability density scale is not shown for the marginal plots, but the distributions are normalized to unit area.

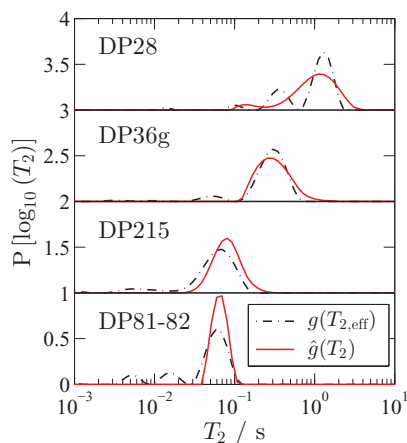


FIG. 18. Transverse relaxation time distributions for porous ceramics saturated with low-salinity brine. Distributions of  $T_2$  (solid red lines) were obtained from optimized  $a$ - $T_2$  distributions. Distributions of  $T_{2,\text{eff}}$  (black dashed-dotted lines) are included for comparison. Legend applies to all plots.

dependence in the diffusion exponent, and hence a single value of  $k_{\text{opt}}$  cannot describe the entire diffusion behavior encapsulated within the data. Notwithstanding, we expect the projected marginal  $\hat{g}(T_2)$  in Fig. 17(c) to be a good representation of the “true” relaxation time distribution based on our simulations in Sec. IV B. The marginal distribution  $h(a)$  is elongated by the variation in diffusion behavior, but this is unimportant as we are concerned only with the determination of  $T_2$ . The resultant  $T_2$  distribution is monomodal, as expected for the porous ceramic sample, with  $T_{2\text{lm}} = 80$  ms. The  $T_{2,\text{eff}}$  distribution (also shown in Fig. 17 c) is, by contrast, bimodal.

The  $T_2$  and  $T_{2,\text{eff}}$  distributions for the four ceramic samples are shown in Fig. 18. The  $T_2$  distributions of samples DP81-82, DP215, and DP36g are all monomodal, and are expected to reflect the pore size distribution of the ceramics.<sup>60</sup> We do not attempt to rescale  $T_2$  to pore size with the usual relationship in Eq. (1) as the ceramics contain different fractions of iron oxide, resulting in a unique (unknown)  $\rho_2$  for each sample.<sup>61</sup> Nevertheless, it is clear that the ceramics with larger pores are characterized by longer  $T_2$  relaxation times as expected. In all the ceramics, the  $T_{2,\text{eff}}$  distributions are multimodal due to the diffusive contribution to the signal decay in the CPMG data, even when acquired with the shortest practical echo time. It is interesting to note that the ceramic sample DP28, having the largest pores, is characterized by a bimodal  $T_2$  distribution. The shape of this distribution is confirmed by measurements of  $T_1$  where a consistent bimodal distribution is observed. As  $T_1$  is known to be independent of diffusion with internal gradients,<sup>16,17</sup> we attribute this bimodal distribution to relaxation occurring in the slow diffusion limit of Brownstein and Tarr<sup>11</sup> (such that  $\rho_2 \ell_s / D \gg 1$ ) where the surface and bulk relaxing spins are not well mixed on the time scale of the NMR experiment, so multiple relaxation modes exist within the pore. Similar behavior has been observed in granular sandstones with large pores and strong surface relaxation.<sup>62</sup>

Although the absolute  $\rho_2$  scaling is unknown for each sample, we can expect the ratio  $\rho_1/\rho_2$  to remain approximately constant as the concentration of paramagnetic impurities varies.<sup>59</sup> Therefore, a constant  $T_1/T_2$  ratio is predicted.

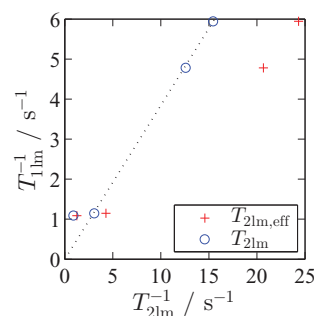


FIG. 19. Correlation between  $T_{1\text{lm}}$  and  $T_{2\text{lm}}$  (blue circles), and between  $T_{1\text{lm}}$  and  $T_{2\text{lm},\text{eff}}$  (red crosses) for brine-saturated porous ceramics, see legend. The ratio  $T_1/T_2 = 2.6$  is indicated by the dotted black line.

In a comparison of  $T_{1\text{lm}}$  and  $T_{2\text{lm}}$ , see Fig. 19, a constant ratio  $T_1/T_2 = 2.6$  describes the relaxation times of the DP81-82, DP215, and DP36g ceramics. The DP28 ceramic exhibits  $T_1/T_2 \approx 1.2$ , which is unsurprising given that relaxation is occurring outside the fast diffusion limit in this sample. In a similar comparison of  $T_{1\text{lm}}$  against  $T_{2\text{lm},\text{eff}}$ , also shown in Fig. 19, we note that the data do not exhibit a single  $T_1/T_{2,\text{eff}}$  ratio.

The results presented here confirm that good approximations to the “true”  $T_2$  distributions have been obtained for the brine-saturated porous ceramics in the presence of diffusion through internal gradients, despite the diffusion exponent in the CPMG data varying as a function of  $t_e$ . These observations suggest that the choice of echo times is not a limiting factor on the determination of  $\hat{g}(T_2)$ , despite the apparent failure of the data collapse plot. The minimization of  $\Phi_{\text{opt}}(k)$  remains a robust method of determining the optimum diffusion exponent when inverting these data.

## C. Portland limestone

In the last example we consider the measurement of relaxation time in a heterogeneous rock. Carbonate formations exhibit pore structures over a hierarchy of length scales, usually characterized as microporosity (e.g.,  $\ell_s \sim 1$   $\mu\text{m}$ ) or macroporosity (e.g.,  $\ell_s > 10$   $\mu\text{m}$ ). Carbonates tend to exhibit small susceptibility contrasts to water,<sup>50</sup> with “clean” formations being diamagnetic. The limestone (predominantly calcium carbonate) chosen for this demonstration is Portland outcrop. The rock plug had dimensions 50 mm  $\times$  38 mm (length  $\times$  diameter) and was saturated with the low-salinity brine described in Sec. V B. The susceptibility contrast between the limestone grains and brine was determined to be  $\Delta\chi = 1.32 \times 10^{-5}$  using a Bartington Instruments MS2C sensor. At a magnetic field strength of  $B_0 = 0.3$  T, the dephasing length was estimated to range from  $\ell_g = 2.6$  to 4.4  $\mu\text{m}$ . In this case, the internal gradient physics of the limestone is expected to be governed by the ST asymptote, at least in the macropores, so these estimates of  $\ell_g$  are considered reliable. CPMG data were acquired with echo times ranging from  $t_e = 160$   $\mu\text{s}$  to 20 ms in 32 logarithmically spaced increments, leading to diffusion path lengths ranging from  $\ell_e = 0.43$  to 7.58  $\mu\text{m}$ . The minimum pore sizes were determined from mercury intrusion porosimetry as  $\ell_s = 0.08$   $\mu\text{m}$

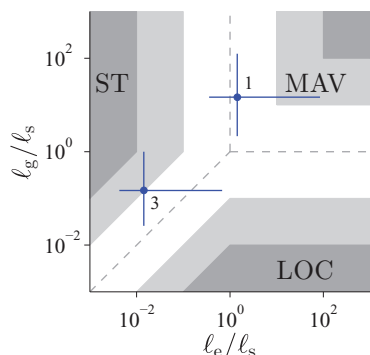


FIG. 20. Schematic illustrating the diffusion regimes ST, MAV, and LOC as defined by the length scales  $\ell_e$ ,  $\ell_s$ , and  $\ell_g$ . The expected diffusion behaviors of low-salinity brine in micropores ( $k = 1$ ) and macropores ( $k = 3$ ) within a limestone plug are indicated by the blue dots. The solid blue lines indicate the maximum expected range of valid diffusion behaviors based on estimates of the diffusion length scales.

and 10  $\mu\text{m}$  for the micropores and macropores, respectively. The pore size was expected to vary over an order of magnitude, with the largest pores estimated at  $\ell_s = 1.2 \mu\text{m}$  and 100  $\mu\text{m}$  for the micropores and macropores, respectively. The corresponding expected range of diffusion behaviors are illustrated in Fig. 20.

Let us first consider the microporosity. We see that  $\ell_s < \ell_g$  and  $\ell_s \sim \ell_e$  at the shortest echo time, so we may expect diffusion in these small pores to occur in the pre-asymptotic MAV regime. In limestone samples containing only microporosity, it has been observed that the contributions from diffusion and surface relaxation are indistinguishable, suggesting that the diffusion is described by the asymptotic MAV regime.<sup>63</sup> We may expect, then, for the signal decay associated with the brine in the microporosity to be governed by a diffusion exponent with  $k = 1$ .

Now we consider the macroporosity. Given the large pore size and weak susceptibility contrast, we may assume diffusion is governed by the ST asymptote. Our estimate of the relevant diffusion regime based on the comparison of  $\ell_e$ ,  $\ell_g$ , and  $\ell_s$  in Fig. 20 supports this assumption, at least for the CPMG data with the shortest echo times. Overall, we have a sample where the diffusive contribution to the CPMG signal decay is governed by two distinct diffusion exponents.

If we invert the CPMG data from the brine-saturated limestone plug, we find a shallow yet distinct minimum in  $\Phi_{\text{opt}}(k)$  at  $k_{\text{opt}} = 1.95$ , see Fig. 21(a). This value of  $k_{\text{opt}}$  is a reasonable average between the extremes of  $k \approx 1$  in the microporosity and  $k \approx 3$  in the macroporosity, based on the simulations in Sec. IV C. Furthermore, the data collapse plot at  $k_{\text{opt}} = 1.95$  in Fig. 21(b) contains features in common with the plots in Fig. 12. Specifically, in Fig. 21(b) the data are seen to collapse at times  $nt_e^{1.95} < 10^{-6} \text{ s}^{1.95}$  and at times  $nt_e^{1.95} > 10^{-3} \text{ s}^{1.95}$ . At intermediate times, however, the data collapse fails. Lacking any further information on the sample,  $k_{\text{opt}} = 1.95$  would be an appropriate choice for generating an  $a$ - $T_2$  distribution, as shown in Fig. 21(c). A sensible  $\hat{g}(T_2)$  marginal distribution is obtained, reflecting the bimodal pore size distribution. Given our expectations of this sample — namely that diffusion should be governed by the

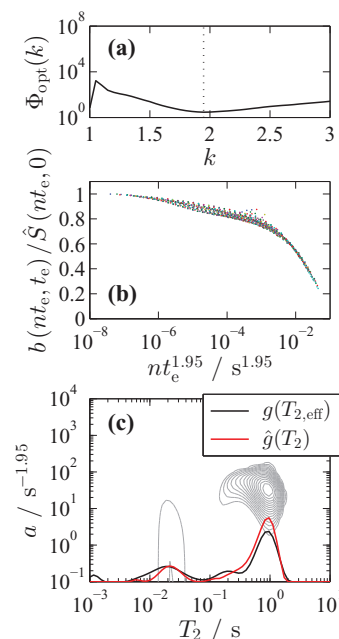


FIG. 21. Process of obtaining the  $T_2$  distribution for a brine-saturated limestone plug. The optimum power in the diffusion exponent  $k_{\text{opt}} = 1.95$  is obtained by minimizing the GCV score; a plot of  $\Phi_{\text{opt}}(k)$  is shown in (a). The data collapse plot obtained at  $k_{\text{opt}}$  is shown in (b). Marker colors indicate different echo times from  $t_e = 0.16$  to 20 ms. An  $a$ - $T_2$  distribution (c) is generated at  $k_{\text{opt}}$  and the marginal distribution  $\hat{g}(T_2)$  (solid red line) is projected from the 2D plot, see legend. For comparison, the estimated  $g(T_{2,\text{eff}})$  distribution (solid black line) is included, calculated from the CPMG decay with the minimum  $t_e = 160 \mu\text{s}$ . The probability density scale is not shown for the marginal plots, but the distributions are normalized to unit area.

ST asymptote in the macropores — we could choose to invert the CPMG data using a diffusion exponent with  $k = 3$ , in which case the  $\hat{g}(T_2)$  distribution is not substantially different from that shown in Fig. 21(c), i.e., the result is insensitive to our choice of  $k_{\text{opt}}$  for  $k \geq 2$ . Out of all the samples studied here, the limestone is unique in that there is negligible difference between the distribution of  $T_2$  (when  $k \geq 2$ ) and the distribution of  $T_{2,\text{eff}}$  at  $t_e = 160 \mu\text{s}$ . Obtaining accurate  $T_2$  distributions in heterogeneous materials is challenging and requires prior knowledge of the rock structure and properties in order to provide a robust interpretation of the data. We will consider the detailed interpretation of  $a$ - $T_2$  distributions in reservoir rocks in a future publication.

## VI. CONCLUSIONS

NMR offers a powerful toolbox for accessing unique information on liquids confined in porous media and the structure of the porous material itself. However, robust interpretation of  $T_2$  distributions in terms of liquid composition and transport, or pore structure, necessitates appropriate data processing. Previously, we introduced a generic model for the diffusion exponent in the form  $-ant_e^k$ , enabling the determination of a 2D  $a$ - $T_2$  distribution.<sup>26</sup> Under ideal conditions, the marginal distribution  $\hat{g}(T_2)$  projected from the  $a$ - $T_2$  plot depends only on spin relaxation, and is independent of diffusion.

In the present work, we have demonstrated that our correction method shows considerable robustness to

measurements where the diffusive contribution to the signal decay depends on multiple asymptotic regimes defined by different values of  $k$ . The assumption that a simple power law describes the diffusion behavior can be violated by the experiment (varying the echo time  $t_e$ ) or by the sample (the characteristic pore sizes  $\ell_s$  span more than an order of magnitude). By simulating CPMG decays, we have shown that accurate  $T_2$  distributions are obtainable under both conditions. To determine  $k_{\text{opt}}$  in these cases, we introduced an automated search based on minimizing the GCV score obtained when inverting CPMG data to form an  $a$ - $T_2$  distribution. This automated method is more efficient than the manual grid search adopted previously, and avoids variability through subjective judgments of experimentalists; the method was validated using a simple water-saturated glass bead pack. Care is required when generating  $a$ - $T_2$  distributions from heterogeneous samples, and prior knowledge of the diffusion length scales  $\ell_e$ ,  $\ell_s$ , and  $\ell_g$  must be obtained using independent analyzes wherever possible to achieve robust and reliable interpretation. Notwithstanding, we have demonstrated the determination of accurate  $T_2$  distributions in complicated porous structures with examples of ceramics used for filtration and catalyst supports, and limestone which forms oil reservoirs or is used in construction. Accordingly, this work expands the range of heterogeneous samples that are now considered appropriate for structural analysis by NMR. In future work we will consider the interpretation of quantitative  $T_2$  distributions in materials of industrial significance.

## ACKNOWLEDGMENTS

The authors thank John Staniland and Laurence Hawkes for assisting with the sample preparation. Edmund Fordham is thanked for helpful discussions.

- <sup>1</sup>J. Mitchell, T. C. Chandrasekera, D. J. Holland, L. F. Gladden, and E. J. Fordham, *Phys. Rep.* **526**, 165 (2013).
- <sup>2</sup>M. D. Mantle and A. J. Sederman, *Prog. Nucl. Magn. Reson. Spectrosc.* **43**, 3 (2003).
- <sup>3</sup>M. D. Mantle, *Int. J. Pharm.* **417**, 173 (2011).
- <sup>4</sup>L. F. Gladden and J. Mitchell, *New J. Phys.* **13**, 035001 (2011).
- <sup>5</sup>J. Mitchell, L. F. Gladden, T. C. Chandrasekera, and E. J. Fordham, *Prog. Nucl. Magn. Reson. Spectrosc.* **76**, 1 (2014).
- <sup>6</sup>Q. Chen and Y. Q. Song, *J. Chem. Phys.* **116**, 8247 (2002); P. Callaghan and I. Furo, *ibid.* **120**, 4032 (2004); Y. Qiao, P. Galvosas, T. Adalsteinsson, M. Schönhoff, and P. T. Callaghan, *ibid.* **122**, 214912 (2005); D. J. Holland, J. Mitchell, A. Blake, and L. F. Gladden, *Phys. Rev. Lett.* **110**, 018001 (2013).
- <sup>7</sup>Q. Chen, A. E. Marble, B. G. Colpitts, and B. J. Balcom, *J. Magn. Reson.* **175**, 300 (2005).
- <sup>8</sup>D. S. Grebenkov, *Rev. Mod. Phys.* **79**, 1077 (2007); R. M. Cotts, M. J. R. Hoch, T. Sun, and J. T. Markert, *J. Magn. Reson.* **83**, 252 (1989).
- <sup>9</sup>P. T. Callaghan, *J. Magn. Reson.* **87**, 304 (1990).
- <sup>10</sup>K. R. Brownstein and C. E. Tarr, *J. Magn. Reson.* **26**, 17 (1977).
- <sup>11</sup>K. R. Brownstein and C. E. Tarr, *Phys. Rev. A* **19**, 2446 (1979).
- <sup>12</sup>E. Grunewald and R. Knight, *Geophysics* **76**, G73 (2011).
- <sup>13</sup>A. A. Peña and G. J. Hirasaki, *Adv. Colloid Interface Sci.* **105**, 103 (2003).
- <sup>14</sup>H. Carr and E. Purcell, *Phys. Rev.* **94**, 630 (1954); S. Meiboom and D. Gill, *Rev. Sci. Instrum.* **29**, 688 (1958).
- <sup>15</sup>Y. Q. Song and P. N. Sen, *Phys. Rev. Lett.* **91**, 029801 (2003); H. Cho and Y. Q. Song, *ibid.* **100**, 025501 (2008).
- <sup>16</sup>J. Mitchell, T. C. Chandrasekera, M. L. Johns, L. F. Gladden, and E. J. Fordham, *Phys. Rev. E* **81**, 026101 (2010).
- <sup>17</sup>R. L. Kleinberg, S. A. Farooqui, and M. A. Horsfield, *J. Colloid Interface Sci.* **158**, 195 (1993); K. E. Washburn, C. D. Eccles, and P. T. Callaghan, *J. Magn. Reson.* **194**, 33 (2008).
- <sup>18</sup>T. C. Chandrasekera, J. Mitchell, E. J. Fordham, L. F. Gladden, and M. L. Johns, *J. Magn. Reson.* **194**, 156 (2008).
- <sup>19</sup>B. Blümich, J. Perlo, and F. Casanova, *Prog. Nucl. Magn. Reson. Spectrosc.* **52**, 197 (2008).
- <sup>20</sup>M. D. Hürlimann, L. Venkataramanan, and C. Flaum, *J. Chem. Phys.* **117**, 10223 (2002).
- <sup>21</sup>Y. Q. Song, L. Venkataramanan, M. D. Hürlimann, M. Flaum, P. Frulla, and C. Straley, *J. Magn. Reson.* **154**, 261 (2002).
- <sup>22</sup>R. L. Kleinberg and M. A. Horsfield, *J. Magn. Reson.* **88**, 9 (1990).
- <sup>23</sup>R. L. Kleinberg, C. Straley, W. E. Kenyon, R. Akkurt, and S. A. Farooqui, SPE paper 26470 presented at the Annual Technical Conference and Exhibition, Houston, Texas, USA, 3–6 October 1993.
- <sup>24</sup>M. D. Hürlimann, A. Matteson, J. E. Massey, D. F. Allen, E. J. Fordham, F. Antonsen, and H. G. Rueslätten, *Petrophysics* **45**, 414 (2004); G. Leu, E. J. Fordham, M. D. Hürlimann, and P. Frulla, *Magn. Reson. Imaging* **23**, 305 (2005).
- <sup>25</sup>L. F. Gladden, C. Buckley, P. S. Chow, J. F. Davidson, M. D. Mantle, and A. J. Sederman, *Curr. Appl. Phys.* **4**, 93 (2004).
- <sup>26</sup>J. Mitchell, T. C. Chandrasekera, and L. F. Gladden, *J. Chem. Phys.* **139**, 074205 (2013).
- <sup>27</sup>J. Mitchell, T. C. Chandrasekera, and L. F. Gladden, *Microporous Mesoporous Mater.* **178**, 20 (2013).
- <sup>28</sup>D. J. Holland, A. J. Sederman, M. D. Mantle, L. F. Gladden, and A. Middelberg, *J. Chromatogr. A* **1033**, 311 (2004).
- <sup>29</sup>A. J. Sederman, P. Alexander, and L. F. Gladden, *Powder Technol.* **117**, 255 (2001).
- <sup>30</sup>V. Tudisca, C. Casieri, F. Demma, M. Diaz, L. Pinñol, C. Terenzi, and F. De Luca, *J. Archaeol. Sci.* **38**, 352 (2011).
- <sup>31</sup>A. J. Bohris, B. Newling, P. J. McDonald, A. Raoof, and N. L. Tran, *J. Mater. Sci.* **33**, 859 (1998).
- <sup>32</sup>S. Muncaci, C. Mattea, S. Stapf, and I. Ardelean, *Magn. Reson. Chem.* **51**, 123 (2013).
- <sup>33</sup>A. J. Sederman, M. D. Mantle, and L. F. Gladden, *Magn. Reson. Imaging* **21**, 359 (2003).
- <sup>34</sup>T. S. Ramakrishnan, L. M. Schwartz, E. J. Fordham, W. E. Kenyon, and D. J. Wilkinson, “Forward models for nuclear magnetic resonance in carbonate rocks,” in *Proceedings of the SPWLA 39th Annual Logging Symposium*, 26–29 May 1998 (Society of Petrophysicists and Well-Log Analysts, 1998); D. F. Allen, A. Boyd, J. Massey, E. J. Fordham, M. O. Amabeoku, W. E. Kenyon, and W. B. Ward, “The practical application of NMR logging in carbonates: 3 case studies,” in *Proceedings of the SPLWA 42nd Annual logging symposium*, 17–20 June 2001 (Society of Petrophysicists and Well-Log Analysts, 2001).
- <sup>35</sup>M. Alesiani, S. Capuani, and B. Maraviglia, *Magn. Reson. Imaging* **21**, 799 (2003); D. Capitani, V. Di Tullio, and N. Proietti, *Prog. Nucl. Magn. Reson. Spectrosc.* **64**, 29 (2012).
- <sup>36</sup>T. M. de Swiet and P. N. Sen, *J. Chem. Phys.* **100**, 5597 (1994).
- <sup>37</sup>P. Le Doussal and P. N. Sen, *Phys. Rev. B* **46**, 3465 (1992).
- <sup>38</sup>J. Mitchell, T. C. Chandrasekera, and L. F. Gladden, *J. Chem. Phys.* **132**, 244705 (2010).
- <sup>39</sup>B. Q. Sun and K. J. Dunn, *Phys. Rev. E* **65**, 051309 (2002).
- <sup>40</sup>M. D. Hürlimann, K. G. Helmer, T. M. de Swiet, P. N. Sen, and C. H. Sotak, *J. Magn. Reson. Ser. A* **113**, 260 (1995).
- <sup>41</sup>L. J. Zielinski and P. N. Sen, *J. Magn. Reson.* **147**, 95 (2000).
- <sup>42</sup>S. D. Stoller, W. Happer, and F. J. Dyson, *Phys. Rev. A* **44**, 7459 (1991).
- <sup>43</sup>J. Mitchell, T. C. Chandrasekera, and L. F. Gladden, *Prog. Nucl. Magn. Reson. Spectrosc.* **62**, 34 (2012).
- <sup>44</sup>L. Venkataramanan, Y. Q. Song, and M. D. Hürlimann, *IEEE Trans. Signal Process.* **50**, 1017 (2002).
- <sup>45</sup>J. Mitchell and E. J. Fordham, *J. Magn. Reson.* **212**, 394 (2011).
- <sup>46</sup>P. C. Hansen, *BIT Numer. Math.* **27**, 534 (1987).
- <sup>47</sup>J. P. Butler, J. A. Reeds, and S. V. Dawson, *SIAM J. Num. Anal.* **18**, 381 (1981).
- <sup>48</sup>G. Wahba and Y. H. Wang, *Commun. Stat. Theory* **19**, 1685 (1990); J. D. Wilson, *J. Mater. Sci.* **27**, 3911 (1992).
- <sup>49</sup>M. J. L. Orr, “Introduction to radial basis function networks,” Technical Report (Centre for Cognitive Science, University of Edinburgh, 1996).
- <sup>50</sup>M. D. Hürlimann, *J. Magn. Reson.* **131**, 232 (1998).
- <sup>51</sup>R. P. Brent, *Algorithms for Minimization without Derivatives* (Prentice-Hall, Englewood Cliffs, New Jersey, 1973).
- <sup>52</sup>R. Vold, J. Waugh, M. Klein, and D. Phelps, *J. Chem. Phys.* **48**, 3831 (1968).
- <sup>53</sup>G. Wahba, *SIAM J. Numer. Anal.* **14**, 651 (1977).



- <sup>54</sup>P. J. McDonald, J. P. Korb, J. Mitchell, and L. Monteilhet, *Phys. Rev. E* **72**, 011409 (2005).
- <sup>55</sup>D. W. Weber, J. Mitchell, J. McGregor, and L. F. Gladden, *J. Phys. Chem. C* **113**, 6610 (2009).
- <sup>56</sup>L. Monteilhet, J. P. Korb, J. Mitchell, and P. J. McDonald, *Phys. Rev. E* **74**, 061404 (2006).
- <sup>57</sup>P. J. McDonald, V. Rodin, and A. Valori, *Cement Concrete Res.* **40**, 1656 (2010).
- <sup>58</sup>E. D. Ostroff and J. S. Waugh, *Phys. Rev. Lett.* **16**, 1097 (1966).
- <sup>59</sup>I. Foley, S. A. Farooqui, and R. L. Kleinberg, *J. Magn. Reson. Ser. A* **123**, 95 (1996).
- <sup>60</sup>D. P. Gallegos, K. Munn, D. M. Smith, and D. L. Stermer, *J. Colloid Interface Sci.* **119**, 127 (1987); D. P. Gallegos, D. M. Smith, and C. J. Brinker, *ibid.* **124**, 186 (1988); S. Davies and K. J. Packer, *J. Appl. Phys.* **67**, 3163 (1990).
- <sup>61</sup>J. Mitchell, S. C. Stark, and J. H. Strange, *J. Phys. D* **38**, 1950 (2005).
- <sup>62</sup>J. Mitchell, *J. Magn. Reson.* **240**, 52 (2014).
- <sup>63</sup>J. Mitchell and E. J. Fordham, *Rev. Sci. Instrum.* **85**, 111502 (2014).